Journal of Mechanical Materials and Mechanics Research

XinJiang Lu — Central South University, China

Venanzio Giannella — University of Salerno, Italy

Nima Ahmadi — Urmia University of Technology, Iran

Mohamed El-Amine Slimani — University of Science and Technology Houari Boumediene, Algeria

Ahmad Mahdian Parrany — Sharif University of Technology, Iran

Jinglun Fu — Chinese Academy of Sciences, China

Ali Abd El-Aty — Seoul National University, Korea

Zichen Deng — Northwestern Polytechnical University, China

Vinothkumar Sivalingam — Shandong University, India

Yu-Chun Kung — NantWorks LLC, United States

Mohammad Nimafar — Islamic Azad University, Iran

Kishore Debnath — NIT Meghalaya, India

Shahriar - Dastjerdi — Islamic Azad University of Shahrood, Iran

Abdelkader Doudou — Mohammed First University, Morocco

Hao Yi — Chongqing University, China

Arash Reza — Islamic Azad University of Ahvaz, Iran

Ambreen Afsar Khan — International Islamic University Islamabad, Pakistan

Afshin --- Zeinedini — Kermanshah Branch, Islamic Azad University, Iran

Saad AbdelHameed EL-Sayed — Zagazig University-Faculty of Engineering, Egypt

Xuejun Jason Liu — University of Wisconsin-Stout, United States

Marcos Rodriguez Millan — Carlos III University of Madrid, Spain

Milon Selvam Dennison — Karpagam Academy of Higher Education, India

Elammaran Jayamani — Swinburne University of Technology Sarawak campus, Malaysia

Matteo Strozzi — Department of Sciences and Methods for Engineering, Italy

Rongyun Zhang — Anhui Polytechnic University, China

Mehdi Safari — Arak University of Technology, Iran

Asim Mukhopadhyay — University of Burdwan, India

Chew Kuew Wai — Universiti Tunku Abdul Rahman (UTAR), Malaysia

Bing Yang — Southwest Jiaotong University, China

Journal of Mechanical Materials and Mechanics Research

Editor-in-Chief

Dr. Jan Awrejcewicz

Contents

Articles

ARTICLE

Thermo-Mechanical Analysis of a Typical Vehicle Engine Using PTC-Creo

Jafar Mahmoudi[*]

Department of Sustainable Production Development, School of Industrial Engineering and Management, KTH Royal Institute of Technology, Stockholm, Sweden

ARTICLE INFO	ABSTRACT
	In this work, a typical vehicle engine is modeled within PTC-Creo software, and its thermal, mechanical, and thermo-mechanical performance are evaluated. This is followed by the vibrational, fatigue, and buckling analysis of the assembly of components, which are the predominant failure causes. The results show that the least temperature gradient occurs in the center of the pin, which connects the piston to the connecting rod, the maximum displacement is seen just below the piston head, and the thermo-mechanical failure is caused mostly (about 85%) by the mechanical load rather than the thermal one. Also, in fatigue analysis, the minimum and maximum values for the safety factor are 0.63 and 5, respectively. The results can prevent the reoccurrence of similar failures and help the enhancement of the components' design and manufacturing process.

1. Introduction

As a power-producer component, the engine has a fundamental and crucial role in vehicles. Analysis of the factors affecting the engine's performance is very important, which should be accompanied by the identification of defects and failures in its components. The major components of an engine are the piston, connecting rod, and crankshaft [1].

The connecting rod transforms the reciprocating motion of the piston into the rotational movement of the crankshaft. These components have relatively complex manufacturing processes and procedures [2], and thus their proper design and analysis are of high importance before

manufacturing, which can prevent the reoccurrence of similar failures [3]. For this purpose, it is imperative to investigate the performance of crucial components under the mechanical and thermal loads along with the consideration of the main potential failures, such as the fatigue failure.

To analyze the performance of an engine's components under different loading scenarios and their possible failures, both experimental and numerical methods are used. While the former approach is valuable, it entails spending high costs in comparison with the latter approach. Among numerical methods, the Finite Element Method (FEM) is a well-established procedure which has a high

simulation capability. Different software such ANSYS, CATIA, MSC/Nastran are utilized in this regard [4,5]. Note that Computer-Aided Design (CAD) is obviously the key component of computerized mechanical engineering. The incorrect or corrupted CAD model causes many problems in Computer-Aided Manufacturing (CAM) and Computer-Aided Engineering (CAE) applications. Typical vehicle main components are given here (Figure 1).

Figure 1. Individual components of the assembly, including piston, connecting rod, pin, and crankshaft

Considering the above explanations, numerous research works have been done on the engine, especially on the crucial components, including piston, connecting rod, and crankshaft. Liu et al. [6] investigated the piston of a diesel engine in different thermal, mechanical, and thermal-mechanical coupling conditions using FEM. Zhaoju et al. [7] calculated the temperature field distribution of a diesel engine piston in static compression state and the thermo-mechanical coupling stress.

The comparisons showed that the mechanical load is the major stress. Gopi et al. [8] determined the structural and thermal stress distribution of piston rings using CATIA and ANSYS. Rajakumar and Karthiyaraj [9] examined the piston's structural and thermal response using FEM method. They compared the results for aluminum alloy, carbon graphite, and tungsten and concluded that either carbon graphite or tungsten can be used instead of aluminum alloy. Another recent work on the piston is done by Deulgaonkar et al. [2], who carried out Failure Mode and Effect Analysis (FMEA) to provide a deeper understanding of the piston failure along with the usage of experimental methods, including Scanning Electron Microscopy (SEM), Energy Dispersive Spectrometry (EDS) and X-Ray Diffraction (XRD).

On the connecting rod, Strozzi et al. [10] examined the potential failures by dividing it into three parts, including the shank, the small and the big ends. Anderson and Yukioka [11] provided the buckling analysis using two primary FEM methods, namely, the eigenvalue and explicit dynamics. Muhammad and Shanono [12] did the static analysis and weight optimization of a connecting rod and recommended the usage of ANSYS software in production companies. Also, some of the reasons for the failure of the connecting rod are mentioned as overloading, bearing failing, uneven changes of the screws as well as faulty setting up or fatigue. Pani et al. [13] evaluated the buckling strength of a connecting rod suffering from hydro-lock failure. They estimated the critical buckling stress using the Merchant-Rankine and slider-crank approaches and resulted that suitable Buckling Safety Factor (BSF) should be regarded based on the maximum buckling stress to avoid such failures. Rezvani et al. [14] analyzed the connecting rod of a failed locomotive engine using a theoretical procedure, experimental modal testing, and FEM-based simulation. They found the natural frequencies and mode shapes of the component and calculated the critical buckling forces. Witek and Zelek [15] performed the failure analysis of the connecting rod of a turbocharged diesel engine using CATIA for geometrical modeling and ANSYS for stress analysis. Andoko et al. [16] also demonstrated that the values of stress and strain are larger in the area near the big end of the connecting rod.

Analysis of crankshafts is also widely carried out in the literature. Rodrigues et al. [17] presented the modal analysis of a six-cylinder crankshaft using both numerical and experimental approaches. Based on the resulted mode shapes and natural frequencies, damping factors were estimated to be used in dynamic analysis. Ang and Ku [18] used SolidWorks and ANSYS for the fatigue and modal analysis of an automotive crankshaft. Kumar et al. [19] analyzed the crankpin failure in a single-cylinder engine. They introduced some potential reasons for the failure of crankshaft assembly and crankpin as, for example, shaft misalignment, improper lubrication, vibration ensued of the bearings, and based on their results, the lower surface hardness was known as the main reason of failure. The paper mentioned the crankpin fillet as the most critical area of the crankshaft [20]. A similar conclusion is stated for the crankshaft of a helicopter engine [21]. Gomes et al. [22] investigated the seven cases of crankshaft's failures in marine diesel engines and listed some of the failure causes, followed by the proposition of some design modifications. Jiao et al. [23] did the modal and fatigue analysis of a crankshaft in addition to the physical and chemical scrutiny and introduced the main cause of crankshaft failure as fatigue resulted from overload. Kubet et al. [24] provided the static, modal, and harmonic analyses. The latter is used to determine the harmful frequencies of vibrations, having the possibility to break the structure.

While the above-mentioned references have made valuable contributions, the present work aims to provide three main contributions: (1) simultaneous analyses of thermal, mechanical, and thermomechanical in an assembly of components, without the dependent analysis of components, as done in most of the given references, (2) consideration of three important failure mechanisms, including the vibration, fatigue, and buckling, being the main failure causes, and (3) using PTC-Creo as both CAD and CAE software that helps to prevent the possible problems of using two different CAD and CAE software. Also, the utilized software has been used in limited works so far [25-27], or used solely as a CAD tool, such as its usage along with ANSYS in reference [25]. For this purpose, initially, the procedure for thermal, mechanical, and thermomechanical analyses is explained. Then, the modal analysis is described, followed by the investigation of two failure mechanisms, i.e., fatigue and buckling. Finally, the results and discussions are provided in Section 4.

2. Modeling

In this section, we provide the CAD modeling and FEA analyses. In this work, CAD and CAE Creo v5.0.2

environments are employed for the physical modeling and simulation of a typical engine. PTC-Creo offers integrated environments for CAD, CAM, and CAE and reduces data losing through the CAD transferring to the CAE tools.

The first step in FEA simulation is to create an accurate CAD file. The assumed system consists of the assembly of the piston, the connecting rod, the pin between the piston and concocting rod, and the crankshaft. The individual 3D models are shown in Figure 2, and the assembly model is illustrated in Figure 3.

The second step is the material assignment. In our analysis, steel is chosen for the crankshaft, and aluminum is used for piston, connecting rod, and pin [28]. The material choice of the components is addressed in several research works [24,29]. Generally, accurate material behavior depends on the strain rate, temperature, material texture, and so on. In this work, some assumptions are considered to simplify this behavior.

The material is supposed to be isotropic with a linear stress-strain response to the forces, and two different failure formulations are selected to discuss. Hence, the material assignment is applied according to Table 1 for aluminum and Table 2 for steel. Typical mechanical properties and the governing equations are given in Figure 4.
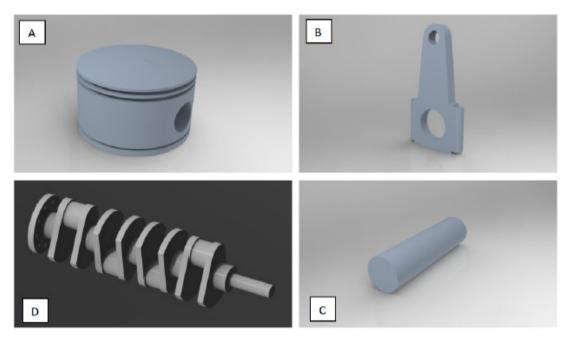

Figure 2. Simulation domain of **i**ndividual components of the assembly, including A) piston, B) connecting rod, C) pin, and d) crankshaft
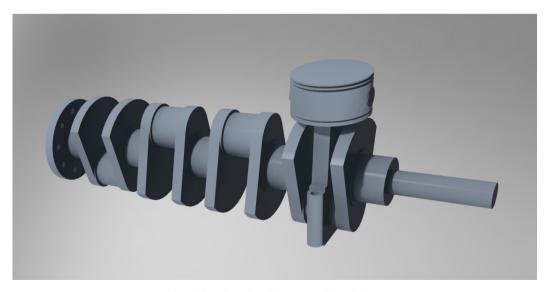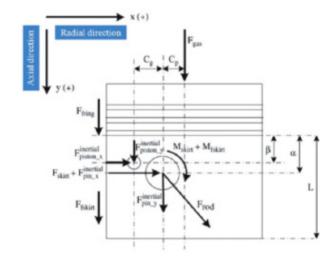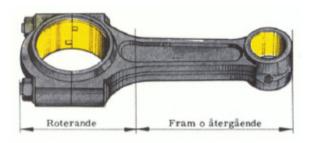

Figure 3. Simulation domain of the aassembly of the components

$$\sum F_y = F_{gas} + F_{f\,ring} + F_{f\,skirt} + F_{inertial\,pin\_y}$$
$$+ F_{inertial\,piston\_y} + F_{rod}\cos\theta = 0$$

$$\sum F_x = F_{skirt} + F_{inertial\,pin\_x} + F_{inertial\,piston\_x}$$
$$- F_{rod}\cos\theta = 0$$

$$\sum M = M_{skirt} + M_{inertial\,piston}$$
$$+ M_{inertial\,piston\_x}(\alpha - \beta)$$
$$+ F_{inertial\,piston\_y}C_g + F_{gas}C_p + F_{f\,ring}C_p$$
$$+ M_f skirt + M_{f\,pin} = 0$$

Material	Density $\rho[kg.m^{-3}]$	Stiffness E [GPa]	Yield stress $\sigma_y[MPa]$	Specific strength $[MPa.m^3/tn]$
Steel 300M	8000	205	1586	198
Aluminium T6	2800	75	413	148
Titanium alloy	4500	115	1000	222
CF weave	1600	70	600	375
CF UD	1600	135	1300	813

Figure 4. Typical mechanical properties and the governing equationas used in this study.

Table 1. Material properties of wrought Aluminum [30]

Specification	Value	Unit
Poisson's ratio	0.33	-
Young's Modulus	7.05e+07	KPa
Thermal expansion coefficient	2.35e-05	1/ºC
Specific heat capacity	8.98e+08	mm²/(s²ºC)
Thermal conductivity	229000	mm kg/(s³ºC)
Density	2.71e-06	kg/mm³
Tensile ultimate strength	290	MPa
Tensile yield strength	185	MPa

Table 2. Material properties of steel [30]

Specification	Value	Unit
Poisson's ratio	0.28	-
Young's Modulus	2e+08	KPa
Thermal expansion coefficient	9.95e-06	1/ºC
Specific heat capacity	4.74e+08	mm²/(s²ºC)
Thermal conductivity	24900	mm kg/(s³ºC)
Density	7.75e-06	kg/mm³
Tensile ultimate strength	500	MPa
Tensile yield strength	350	MPa

The third step is defining the type of analysis. All of the contact areas between the components are assumed as bounded. This means the non-linearity is neglected due to simplification. In this work, thermal, mechanical, thermo-mechanical, fatigue, buckling, and frequency analyses are discussed. Then, the related boundary conditions and loads are specified.

For the thermal analysis, using the convection coefficient of the utilized metals, boundary conditions are considered for their free contact with the air. Table 3 shows the related values. Also, the power consumption of the engine is assumed about 1000 watts.

Table 3. Boundary conditions of the thermal simulation

Part Name	Value	Material
Convection coefficient of piston	250 watt/m²c²	Al
Convection coefficient of pin	270 watt/m²c²	Al
Convection coefficient of connecting rod	200 watt/m²c²	Al
Crankshaft	100 watt/m²c²	Steel
Reference temperature	25 °C	-
Head load on piston head	1000 Watt	-

For the mechanical analysis, it is supposed that two forces, i.e., a 6 MPA load on the piston head combined with gravity, apply to the whole assembly. Table 4 showed the boundary condition of the simulation [28]. As Figures 4-5 show, both rotational and transitional freedoms are constrained from the end and start of the crankshaft. In

this study, the failure index is also measured as a function of Tresca criteria.

Table 4. Boundary conditions of mechanical simulation

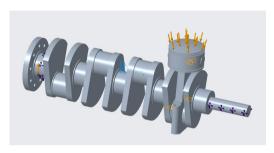| Specification	Value	Unit
Load	104	Kg
Heat transfer coefficient	17	W/m^2*K
Reference temperature	25	°C
Mechanical load	6	MPa
Gravitational acceleration	9.8	m/s^2

Figure 5. The mechanical analysis boundary condition

The third simulation is the thermomechanical analysis, considering the mechanical load and the thermal load of the first simulation simultaneously. All of the boundary and material conditions are the same as the previous related tables (Tables 3-4).

In order to find the damping time of the system, a dynamic study is required. Because of the superiority of modal analysis to dynamic simulation in PTC-Creo and to get some information about the resonance frequencies, firstly, modal analysis is provided. Table 5 shows frequencies and corresponsive mode shape numbers. While each mode shape and resonance frequency have their importance, the first mode shape is the lowest and thus the critical one. After modal analysis, dynamic simulation is used to find the stress variation with respect to time considering a certain damping ratio.

Table 5. Frequencies and corresponsive mode shape number

Mode shape No.	Frequency
Modes shape 1	276.993 Hz
Modes shape 2	452.868 Hz
Modes shape 3	547.086 Hz
Modes shape 4	608.385 Hz

The next step is the important fatigue analysis, which is described as the cause of most crankshafts' failures in a recent review paper by Jiregna et al. [31]. It examines the susceptibility of the model to fatigue damage when subjected to a varying load. In this study, the stress cycles are assumed regular because of the constant speed of the crankshaft. Hence, constant amplitude loading is employed. Firstly, a static analysis is carried out, and the resulted stresses are multiplied by the load factors, chosen from the range of zero to one. Materials are assumed isotropic with the same properties as Tables 3-4.

The fatigue properties are derived from the Uniform Material Law (UML), proposed by Baumel & Seeger [32] to estimate the fatigue life of aluminum and titanium alloys and extended to high-strength steels [33]. The surface of all components is assumed as well-finished, and the failure strength reduction factor is used to reduce the endurance limit. It takes into account for un-modeled stress concentrations, supposed as 1. Also, the desired endurance is envisioned.

Finally, an investigation of buckling is followed. Creo Simulate determines a buckling load factor (BLF) and the corresponding mode form for each case of buckling. It gives the BLF values using two methods. Next, a static study is needed in which Creo measures the model's pressure stiffness due to the applied forces. After that, according to the geometry and product properties, buckling analysis is used to determine the elastic strength of the prototype. Such an examination is a linear bifurcation instability analysis of its value [34]. Large displacement or non-linear buckling investigations may yield significantly different results, depending on the model type and loads being examined.

3. Results and Discussion

In this section, the results of the above-mentioned analyses are provided in the same order as Section 2. For the thermal analysis, the temperature distribution and gradient are shown in Figure 6.

As seen in this figure, the maximum temperature is about 396 °K. Also, the least temperature gradient is in the center of the pin, which connects the piston to the connecting rod. Similar results on the thermal analysis are reported [35]. For the mechanical analysis, Figure 7 (a and b) shows the Von-Mises stress distribution of the assembly after applying the loads. Most of the stress concentration is focused on the sharp corners, which is about 2.94 KPa. It is seen that the maximum value of this factor is around 1.8, concentrated in the sharp corners of the crankshaft. Displacement distribution is also shown in Figure 8. As expected, maximum displacement occurs just below the piston head and is about 0.94 mm.

For the thermomechanical analysis, Figure 9a indicates the displacement distribution. Maximum displacement occurs on the head of the piston, which is about 1 mm. Figures 9b and cc show the Von-mises stress and Tresca failure index distribution, respectively. It is clear that the maximum stress is about 2.91 KPa, the maximum failure
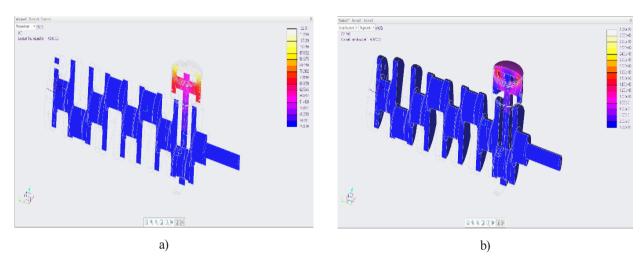
a)

b)

Figure 6. Thermal analysis: (a) Temperature distribution on the half-transparent model, and (b) temperature gradient
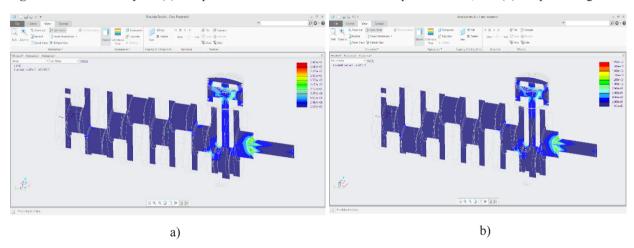

a)

b)

Figure 7. Mechanical analysis: (a) Von-Mises stress distribution, and (b) Tresca failure index distribution
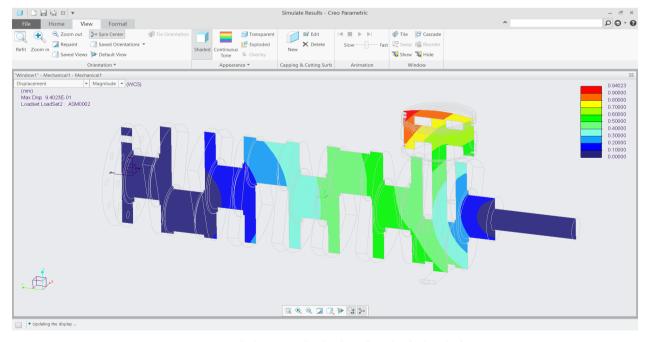

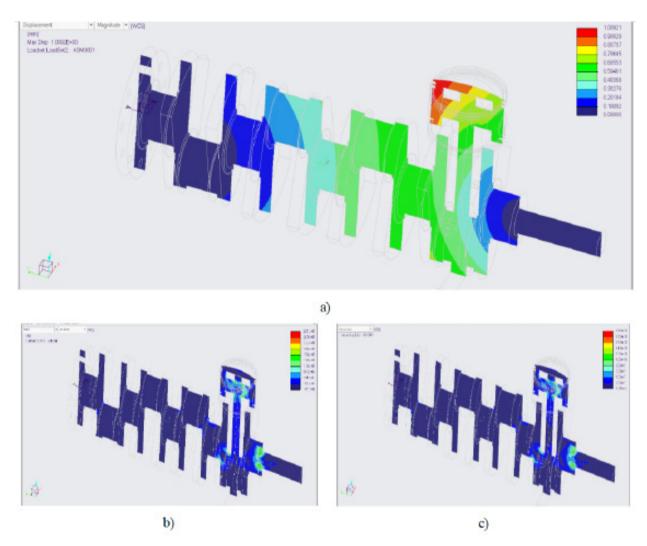**Figure 8.** Displacement distribution of mechanical analysis

Figure 9. Thermomechanical analysis: (a) Displacement distribution of the thermomechanical simulation, (b) Von-mises stress thermomechanical simulation, and (c) Tresca Failure Index Thermomechanical

index (minimum safety factor) is about 1.8, and both of them are located in sharp corners. Similar results are reported [6] for the displacement and stress analysis of the connecting rod.

Figure 8 shows the mode shapes of 1 to 4, respectively. Figure 10 represents the dynamic response history. In this figure, the vertical axis is stress, and the horizontal axis is time. Visibly, the maximum stress happens after approximately 0.001 seconds and with damping ratio 39%, it goes steady on 0.004 seconds. From the modal analysis, it is clear that there are some resonance frequencies from 276 Hz to 608 Hz (Table 5). The rotation per minute of the crankshaft could be different and must be simulated for different speeds. Although it is not sometimes possible to avoid the resonance, the designer must therefore apply a particular procedure, for example, fast-changing of crank-

shaft's RPM when it comes to the resonance speed.

Results of fatigue analysis are provided in Figure 12 show the thermo-mechanicals analyse of different components in general assembly, and it is the ratio of the accumulated fatigue cycles and the total number of cycles to failure. Failure is indicated by a value greater than one. For example, a value of 0.5 represents a loss of 50% in the model's useful life. Due to the exponential nature of fatigue, expressing the ratio of damage in a logarithmic form is useful. Accumulated cycles of fatigue are the number of periods that the system encounters before the study of fatigue is carried out. Figure 10b shows the logarithm of life, and it estimates the number of cycles until the model breaks. In this case, the grey color is 10^{20}, and the red is 10^4 number of cycles.
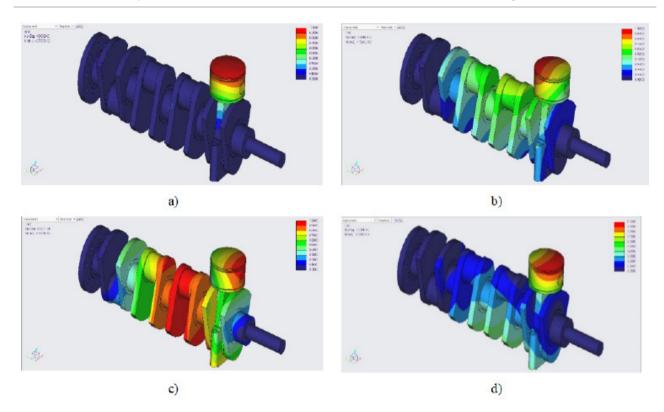
Figure 10. Modal analysis: (a) mode shape 1, (b) mode shape 2, (c) mode shape 3, and (d) mode shape 4.
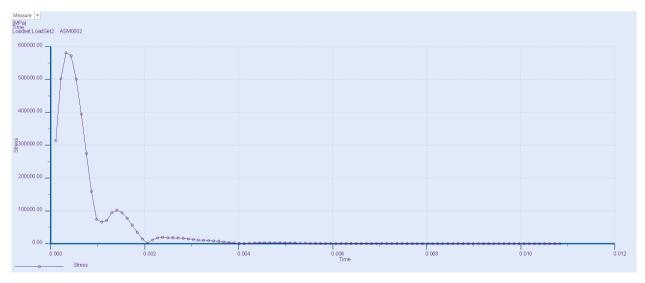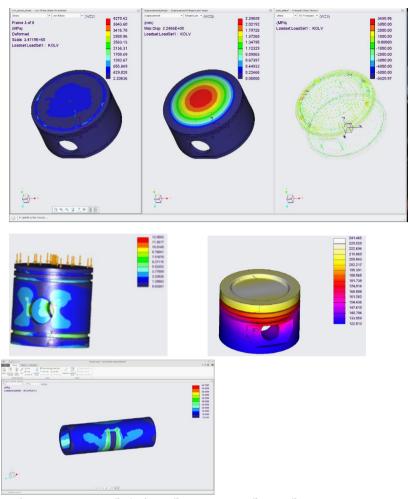
Figure 11. Time vs. Stress Dynamic Time

Figure 13 shows the thermo- mechanicals analyse of the connecting rod.

In PTC-Creo simulation, when the fatigue life calculated for the model is greater than the target design life, the software carries out a back-calculation to determine a permissible SF on the input load. As Figure 10c illustrates, 0.63 and 5 are the minimum and maximum values for the SF in fatigue analysis, respectively. Again, the sharp corners have absorbed the failure.

Figure 14 shows the confidence of life, which is the ratio of the calculated life to the targeted design life, i.e., the desired endurance. Values below one show failure, and those above three usually reflect a reasonable trust to achieve the desired target. The software displays life confidence resulting in a tri-colored fringe to provide an overview of where the model breaks first and the model endures more cycles. Red means life confidence from 0 cycles to the number of cycles obtained for optimal endur-

Accumulated cycles of fatigue are the number of periods that the system encounters before the study of fatigue is carried out. Figure 10b shows the logarithm of life, and it estimates the number of cycles until the model breaks. In this case, the grey color is 10^{20}, and the red is 10^4 number of cycles.
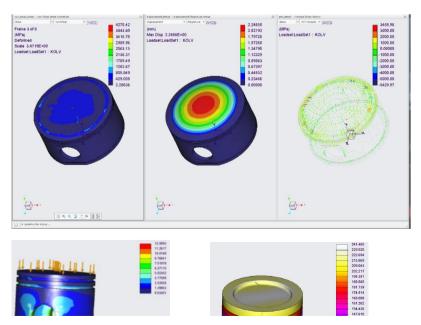

Figure 12. Thermo- mechanicals analyse of different components in general assembly.
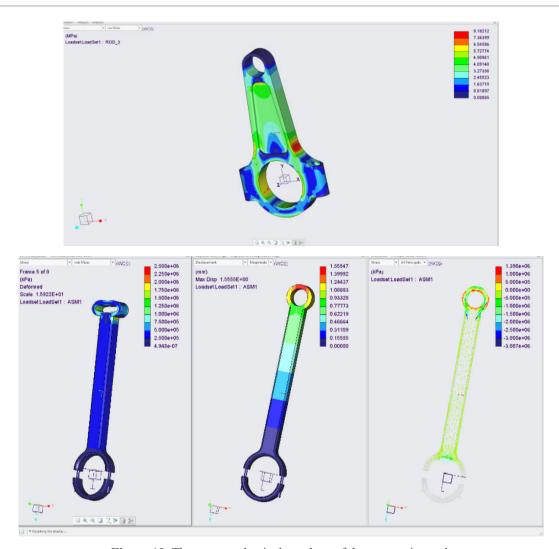
Figure 13. Thermo- mechanicals analyse of the connecting rod.
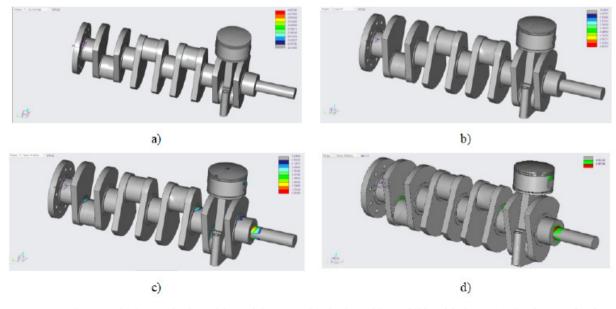
Figure 14. Fatigue analysis: (a) the logarithm of damage, (b) the logarithm of life of fatigue, (c) the factor of safety of fatigue, and (d) the confidence of the life

ance. Yellow means confidence of life varying from the cycle numbers of the optimal endurance to three times of that value. Also, green means any amount of nominal life cycles.

Figure 15 (a-e) shows the mode shapes 1 to 4, respec-

tively. The buckling load factor is also available in Table 6. Regarding previous discussions and this table, mode shapes 1, 2, and 3 are greater than 1, so buckling does not occur. The last one is smaller than −1, in which buckling is avoided again.

a)

b)

c)

d)

e)
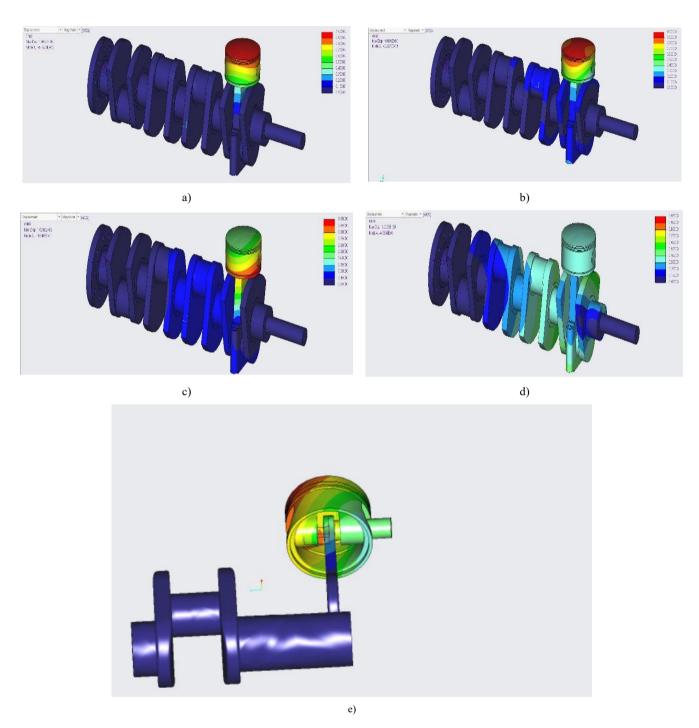
Figure 15. Bucking analysis: (a) Displacement in buckling mode shape 1, (b) Displacement in buckling mode shape 2, (c) Displacement in buckling mode shape 3, and (d and e) Displacement in buckling mode shape 4.

Table 6. BLF and corresponding mode shapes

Mode Shape	Buckling Load Factor
1	5.72
2	22.27
3	45.96
4	–46.33

Figures 16 (a-e) show the displacement, maximum principle thermal stress, Von-mises thermal stress, and failure index thermal stress, respectively. Comparing the results from ther-

mal stress and thermo-mechanical simulations, as Figure 16 shows, 0.12 mm is the maximum displacement caused by the thermal load. Considering Figure 9 from thermo-mechanical simulation, it is concluded that temperature has a 10% contribution in displacement. Also, comparing Figure 16a and Figure 16c shows that heating has participated 15% in stress. Finally, based on Figure 16d and e, failure in the thermo-mechanical case is caused 85% by mechanical load. Such a conclusion on the primacy of the mechanical load is reported [7] for thermo-mechanical loadings.
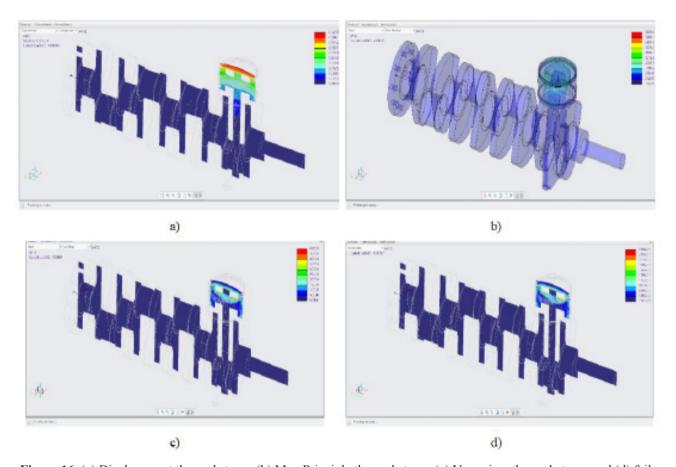
Figure 16. (a) Displacement thermal stress, (b) Max Principle thermal stress, (c) Von-mises thermal stress, and (d) failure index thermal stress.

5. Conclusions

In this study, a typical vehicle engine is simulated and analyzed under the thermal, mechanical, and thermo-mechanical loads. Also, the effects of different parameters on engine failure are investigated. The results showed that the maximum temperature is about 396 °K, the least temperature gradient is at the center of the pin which connects the piston to the connecting rod, most of the stress concentration is focused on the sharp corners, maximum displacement occurs just below the piston head, and the

maximum failure index (minimum SF) is about 1.8. Besides, according to the dynamic response history, the maximum stress happened after approximately 0.001 seconds, the minimum and maximum values for the SF in fatigue analysis are 0.63 and 5, respectively, and the failure in the thermo-mechanical case is caused 85% by mechanical load rather than the thermal one.

It was seen that because of the greater impact of mechanical loads on the design process, mechanical forces and thermal stress effects on other parts should not be neglected. Expectedly, the sharp corners have more possibil-

13

ity to failure rather than round one. Therefore, these areas should be given more attention. In addition to reducing sharp corners as much as possible (e.g., more rounding of the connecting rod's radius [36]), design and manufacturing strategies such as shot peening should be used to prevent the accumulation of stress in critical areas, thereby increasing fatigue strength as well as preventing damage to a large extent. The results provide a basis for the theoretical analysis for the reliability of a typical vehicle engine.

Conflict of Interest

There is no conflict of interest.

References

[1] Hermawan, M.V., Anggono, A.D., Siswanto, W.A., et al., 2019. The Influence of Material Properties to the Stress Distribution on Piston, Connecting Rod and Crankshaft of Diesel Engine. International Journal of Mechanical & Mechatronics. 19(6), 13-26.

[2] Deulgaonkar, V.R., Ingolikar, N., Borkar, A., et al., 2021. Failure analysis of diesel engine piston in transport utility vehicles. Engineering Failure Analysis. 120, 105008.

[3] Xu, X.L., Yu, Zh.W., 2018. Failure analysis of a truck diesel engine crankshaft. Engineering Failure Analysis. 92, 84-94.

[4] Zhang, M.Q., Zhao, Ch., Yan, Zh.Q., et al., 2019. The Structure, Stress and Modal Analysis of 1.6-Liter Gasoline Engine Connecting Rod Based on Finite Element Analysis. IOP Conference Series: Materials Science and Engineering. 677(3), 032094.

[5] Viet Nguyen, D., Duy, V.N., 2018. Numerical analysis of the forces on the components of a direct diesel engine. Applied Sciences. 8(5), 761.

[6] Liu, X., Wang, Y., Liu, W., 2017. Finite element analysis of thermo-mechanical conditions inside the piston of a diesel engine. Applied Thermal Engineering. 119, 312-318.

[7] Qin, Zh.J., Li, Y.S., Yang, Zh.Zh., et al., 2019. Diesel engine piston thermo-mechanical coupling simulation and multidisciplinary design optimization. Case Studies in Thermal Engineering. 15, 100527.

[8] Gopi, E., Saleem, M., Chandan, S., et al., 2019. Thermal and static analysis of engine piston rings. International Journal of Ambient Energy. 1-5.

[9] Rajakumar, S., Karthiyaraj, M., 2020. A comparative study of structural and thermal analyses on piston materials. International Journal of Scientific Development and Research (IJSDR). 5(12).

[10] Strozzi, A., Baldini, A., Giacopini, M., et al., 2016. A repertoire of failures in connecting rods for internal combustion engines, and indications on traditional and advanced design methods. Engineering Failure Analysis. 60, 20-39.

[11] Anderson, A., Yukioka, M., 2012. Connecting rod buckling analysis using eigenvalue and explicit methods. No. 2012-32-0102. SAE Technical Paper.

[12] Muhammad, A., Shanono, I.H., 2019. Static analysis and optimization of a connecting rod. Journal of Engineering and Technological Sciences. 6(1), 24-40.

[13] Pani, A.R., Patel, R.K., Ghosh, G.K., 2020. Buckling analysis and material selection of connecting rod to avoid hydro-lock failure. Materials Today: Proceedings. 27, 2121-2126.

[14] Rezvani, M.A., Javanmardi, D., Mostaghim, P., 2018. Diagnosis of EMD645 diesel engine connection rod failure through modal testing and finite element modeling. Engineering Failure Analysis. 92, 50-60.

[15] Witek, L., Zelek, P., 2019. Stress and failure analysis of the connecting rod of diesel engine. Engineering Failure Analysis. 97, 374-382.

[16] Andoko, A., Nauri, I.M., Paryono, P., et al., 2020. Failure analysis on the connecting rod by finite element method. AIP Conference Proceedings. 2262(1), 040011.

[17] Rodrigues, A., Silva, R.L., Cruz, R., et al., 2011. Experimental and numerical modal analysis of 6 cylinders diesel crankshaft. No. 2011-36-0358. SAE Technical Paper.

[18] Ang, Y.Z., Pei, X.K., 2021. Study on Failure Analysis of Crankshaft Using Finite Element Analysis. MATEC Web of Conferences. 335, 03001. EDP Sciences.

[19] Kumar, M., Senthil, S.R., Suresh, M., 2014. Analysis of crankpin failure in a single cylinder engine. International Journal of Mechanical Engineering and Robotics Research. 3(4), 260.

[20] Sola, J.F., Alinejad, F., Rahimidehgolan, F., et al., 2019. Fatigue life assessment of crankshaft with increased horsepower. International Journal of Structural Integrity.

[21] Infante, V., Freitas, M., Fonte, M., 2019. Failure analysis of a crankshaft of a helicopter engine. Engineering Failure Analysis. 100, 49-59.

[22] Gomes, J., Gaivota, N., Rui, F.M., et al., 2018. Failure analysis of crankshafts used in maritime V12 diesel engines. Engineering Failure Analysis. 92, 466-479.

[23] Jiao, A.Y., Liu, B.H., Chen, X.M., et al., 2020. Fracture failure analysis of KL crankshaft. Engineering Failure Analysis. 112, 104498.

[24] Kurbet, S.N., Kuppast, V.V., Talikoti, B., 2020. Material testing and evaluation of crankshafts for structural analysis. Materials Today: Proceedings.

[25] Kumar, K.S., 2016. Design and Analysis of IC Engine Piston and Piston-Ring on Composite Material Using Creo and Ansys Software. Journal of Engineering and Science. 1(1), 39-51.

[26] Prasad, D.R., Naga, Ch.S., 2017. Design and Analysis of 150CC IC Engine Connecting Rod. International Journal of Scientific Engineering and Technology Research 6(17), 3397-3402.

[27] Bedse, U.A., 2016. Developing a GUI based Design Software in VB Environment to Integrate with CREO for Design and Modeling of CI Engine. International Journal of Latest Trends in Engineering and Technology (IJLTET). 6(4).

[28] Yang, J., Wang, Y., Xiao, M.W., 2011. Heat load analysis of piston based on the ANSYS. Advanced Materials Research. 199, 1192-1195.

[29] Citti, P., Giorgetti, A., Millefanti, U., 2018. Current challenges in material choice for high-performance engine crankshaft. Procedia Structural Integrity. 8, 486-500.

[30] Ellis, D.E., 1960. Mechanical properties of aluminum alloys at various temperature *S*. No. NAA-SR-Memo-5716. Atomics International. Division of North American Aviation, Inc., Canoga Park, California.

[31] Sirata, G.G., 2020. Fatigue Failure Analysis of Crankshafts-A Review. IJISET-International Journal of Innovative Science, Engineering & Technology. 7(5).

[32] Baumel Jr, A., Seeger, T., 1990. Materials data for cyclic loading. Supplement 1. Elsevier Science Publishers, P. O. Box 211, 1000 AE Amsterdam, The Netherlands.

[33] Korkmaz, S., 2010. Uniform material law: extension to high-strength steels: a methodology to predict fatigue life of high-strength steels. VDM.

[34] Zienkiewicz, O.C., Taylor, R.L., 1977. The Finite Element Method, Third editions.

[35] Jangam, S.P., Kumar, S., Maheshwari, S., 2018. Literature review on analysis of various components of IC engine. Materials Today: Proceedings. 5(9), 19027-19033.

[36] Rakic, S., Bugaric, U., Radisavljevic, I., et al., 2017. Failure analysis of a special vehicle engine connecting rod. Engineering Failure Analysis. 79, 98-109.

ARTICLE

Thermomechanical and Flow Analysis of a Typical Truck Radiator Using PTC-Creo

Jafar Mahmoudi[*]

Department of Sustainable Production Development, School of Industrial Engineering and Management, KTH, Sweden

ABSTRACT

In automobile engines, it is commonly known that the proper removal of the excess heat, resulting from internal combustion, is of high significance in the prevention of numerous negative consequences. In this regard, the radiator has a pivotal role as the main component of the engine's cooling system. Hence, its design and analysis are highly important, requiring more comprehensive failure and flow investigations. In this work, a Scania radiator is examined under the thermal and mechanical loads, followed by its analysis under the combined thermomechanical loading. Then, the flow characteristics, including the velocity, pressure, and enthalpy, are studied. In this regard, PTC-Creo software is utilized. The results demonstrate that thermal stress causes seven times more displacement than a mechanical one. When they are combined, this value reaches 1.5 mm. Also, the maximum failure index value of the Tresca theory is around 4.58, observed at the inlet side of the radiator. Besides, this paper indicates that the PTC-Creo can be considered a reliable and economical tool for the simulation of industrial applications, such as the considered radiator of a heavy-duty cooling system.

1. Introduction

The demand for more efficient and powerful engines in smaller hood spaces has caused a problem in the proper heat loss of automotive heat exchangers. As we know, in cars, the fuel and air produce power through the combustion inside the engine. Only a fraction of the total generated power is supplied to the car as power, and the rest is wasted. It is known that 33% of the energy generated by the engine is lost in heat form. If this excess heat is not removed, the engine temperature will become too high, leading to the engine overheating, which in turn causes the breakdown of the lubricating oil, weakening of the metal in engine parts, and considerable wear between the parts [1]. To minimize the pressure and stress on the engine due to heat generation, car heat exchangers must be redesigned to be more compact while maintaining a high level of heat transfer performance. A well-known type of heat

---

*Corresponding Author:

Jafar Mahmoudi,

Department of Sustainable Production Development, School of Industrial Engineering and Management, KTH, Sweden;

Email: Mahmoudi@kth.se

exchanger is a radiator.

A radiator is a heat exchanger used in heating and cooling systems to transfer heat energy from one medium to another. Most radiators are designed and built to be used in cars and buildings and usually function as a water temperature carriers. Figure 1 shows a typical truck radiator.

Figure 1. Typical Truck Radiator

Their structure is such that the liquid circulates in their pipes and causes the environment to heat or cool [2,3]. They are made of different materials, including aluminum, steel, copper, and cast iron. In terms of heat transfer, copper can be said to have the best transfer, but due to its very high cost, it is not economical to use. After copper, aluminum has the best heat transfer that does not rust. Most modern cars use aluminum radiators. These radiators are made by soldering thin aluminum fins to the flattened aluminum tubes [4]. The coolant passes through many tubes mounted parallel from the inlet to the outlet. The fins conduct the heat of the tubes and transfer it to the air passing through the radiator. Therefore, proper analysis of the radiator is vital in order to accomplish high-performance designs.

Numerous research works have been done on the radiator of automobile engines in various aspects. Aravindkumar et al. [5] examined a radiator tube with varying geometries using different nanofluids. The geometries were the straight and spiral tubes, designed with Catia, and the nanofluids included, for example, beryllium, oxide, copper oxide, silicon carbide, and tin oxide. They depicted the contours of static pressure and velocity vectors and then concluded that the spiral flow and the copper oxide are the best choice for the radiator's geometry and nanofluid, respectively. Sheikhzadeh et al. [6] investigated the thermal performance of a car radiator using Ethylene Glycol/copper nanofluid in various environmental conditions. They showed that increasing the volume fraction values of nanoparticles and Reynolds number of the inlet air leads to a increase of the heat transfer rate. Besides,

adding nano-sized particles to the radiator coolant fluid can significantly reduce its output temperature. Moreover, a review work is presented on the application of nonfluids in the automotive radiator by Maysam Molana [7]. Another similar work has been recently done [8], addressing the hybrid nanofluids.

Rinu Sathyan [9] compared the ordinary straight tube of the radiator with the helical type. The author used Solid-Works for modeling and ANSYS for fluid flow analysis. He provided the temperature distribution for different mass flow rates and concluded that the proposed design is preferable to the straight type due to the better performance and size. Chidley et al. [10] carried out the thermo-mechanical analysis of automotive heat exchangers using Comsol. They used InfraRed thermography to record the thermal history of the radiator, along with the adoption of an energetic fatigue criterion. Similar work is done by Roger and Chidley [11] as well. Gu et al. [12] addressed the tank leakage of aluminum alloy radiator due to corrosion. Baou et al. [13] tried to enhance the radiator performance using different porous fin configurations and materials. They resulted that the corrugated pattern provides the best thermal performance among the considered geometries, and the horizontal configuration leads to the lowest pressure loss. Also, it was demonstrated that using porous media in the radiator channels improves its overall thermal performance factor by up to 237%. The resulting technical drawing is shown in Figure 2.
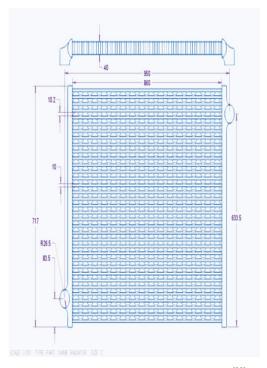

Figure 2. Technical drawing geometry [22]

Kim et al. [14] proposed a numerical method for the determination of temperature distribution in automobile radiators without requiring a prototype model. Amrutkar et al. [15] performed the theoretical, numerical, and experimental heat transfer analyses of a radiator. They used ε-NTU method to describe the heat transfer calculations and to determine the radiator size. Sahriff et al. [16] studied the fins' effects on the car radiator performance under the atmospheric temperature of Kano State of Nigeria. Honda Civic 2000 car radiator was modeled in SolidWorks and simulated in ANSYS with water as the cooling fluid. Their results showed a 25% decrease in the outlet temperature in the case of attaching fins to the radiator. Regarding energy dissipation, the finned radiator dissipates 74% of the cooling energy, while the radiator without a fin dissipates only 40.8%. Mia and Hossen [17] provided the CFD analysis of a radiator tube with fin using ANSYS FLUENT. The authors represented the variations of pressure drop, temperature difference, and velocity contours. They observed the great effect of the volume fraction of nano particles and Reynold number on the preferred temperature and pressure.

Patel et al. [18] carried out the heat transfer analysis of a car radiator with different mass flow rates of the coolant using an ANSYS workbench. Kasu et al. [19] designed a radiator using SolidWorks, performed CFD analysis and compared it with experimental results. In addition to the above research works, there are two studies examining the radiator in a different way. Marc Bonato [20] studied a brazed aluminum alloy car radiator undergoing thermomechanical loadings. He intended to determine the effect of the manufacturing process on the durability of the component in the field. The author concluded that the brazing process is well-controlled in all production units and for different radiator technologies. Goyal et al. [21] researched the reliability measures such as the availability, reliability, and MTTF of the automotive water cooling system considering the time and its failure rate parameters using Markov process and supplementary variable technique. Also, they investigated the sensitivity of these reliability characteristics to enhance the functioning of the water cooling system.

While the above-mentioned references have made valuable contributions, the present work aims to provide three main contributions: (1) simultaneous analyses of thermal, mechanical, and thermomechanical with the determination of the failure index based on the Tresca theory, (2) presentation of the flow characteristics including the velocity, temperature, and enthalpy, (3) using PTC-Creo as both CAD and CAE software. To the knowledge of the author, the utilized software has not been used for the analysis of car radiators, and there are limited papers examining the capability of this software in industrial applications. For this purpose, initially, the modeling procedure, including the thermal, mechanical, and thermomechanical analyses, is explained in Section 2. Then, the related results and discussions are provided in Section 3.

An internal combustion engine (piston engine) is a type of heat engine whose task is to convert supplied heat into mechanical energy [22]. When the fuel is burned, heat is developed which is absorbed by gas enclosed in a cylinder. When the gas is heated, the pressure rises, which in turn pushes the piston outwards and thus mechanical work is performed.

Very high temperatures occur in the combustion chamber, between 1800 °C to 2200 °C [22]. Therefore, cooling of the cylinder walls, cylinder head, piston top, etc. is required. The gas temperature is higher in otto engines (gasoline engines) than in diesel engines. About 20%~30% of the amount of heat supplied by the fuel is removed by cooling.

The cooling can be done by either water or air cooling. As air has a significantly lower cooling capacity than water, air cooling only occurs in small engines and aircraft and motorcycle engines. With water cooling, water circulates in a closed system through the engine's cooling channels. Cooling water absorbs heat that is emitted to the surroundings via the radiator itself.

2. Modeling Procedure

In this section, the procedure to analyze the chosen radiator, as shown in Figure 3, is explained. The First step is to make an accurate CAD file for the FEA simulation, which is carried out in the PTC-Creo Part environment.

The second step is the material assignment. Aluminum alloys are utilized widely for radiators [24]. While Aluminum 1050 has a higher thermal conductivity value (229 W/m*K), it has weak mechanical properties [25]. To get better mechanical feedback, the 6xxx series of aluminum alloys are commonly used, and their thermal conductivity values depend on the temperature of the alloy. Also, in general, accurate material behavior is dependent on the strain rate, temperature, material texture, and so on. In this work, some assumptions are applied to simplify this behavior. The material is supposed to be isotropic with a linear stress-strain response to the forces. Two different failure formulations are selected to discuss as well. Table 1 shows the specifications of the considered material.
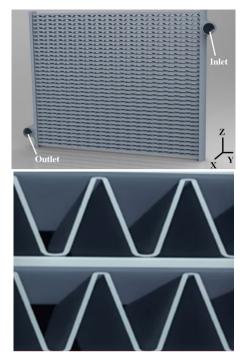
Figure 3. Simulation Domain Radiator [23]

Table 1. Material properties of the wrought aluminum [25]

Specification	Value	Unit
Poisson's ratio	0.33	-
Young's Modulus	7.05e+07	KPa
Thermal expansion coefficient	2.35e-05	1/°C
Specific heat capacity	8.98e+08	mm^2/(s^2 °C)
Thermal conductivity	229000	mm kg/(s^2 °C)
Density	2.71e-06	Kg/mm^3
Tensile ultimate strength	290	MPa
Tensile yield strength	185	MPa

The third step is to define the type of analysis. In the current study, three simulations, including thermal, mechanical, and thermomechanical analysis of the radiator, are discussed.

General assumptions are [26]:

(1) The mass flow rate, material properties, and surface temperature are constant.

(2) The contact air has constant behavior.

(3) The flow is assumed to have a uniform inlet velocity of 1 m/s and an outlet one of about 0.83m/s.

(4) All the mechanical and thermal loads are uniformly applied to the model.

(5) Fixture locations are supposed rigid, and it may cause some concentration of stress there.

For the thermal stress analysis, at first, the thermal load of the radiator and its effect is intended. The inlet and outlet temperatures are 100 °C and 40 °C, respectively. This temperature causes displacement, and when the radiator is assumed fixed from the inlet and outlet locations, stress appears. The heat transfer coefficient for the radiator combined with a fan is supposed as 70 w/m^2*K [27]. Bounded interfaces and rigid body assumptions are considered for the radiator model. The summary of boundary conditions applied to the model is shown in Table 2.

Table 2. Boundary conditions of the thermal simulation [25]

Specification	Value	Unit
Inlet temperature	100	°C
Outlet temperature	40	°C
Heat transfer coefficient	70	W/m^{2}K
Reference temperature	25	°C

The second FEA simulation is the investigation of mechanical loads on the radiator. The gravity and static loads are applied, resulting from the weight of parts connected to the radiator. The radiator is assumed fixed from the inlet and outlet locations in the static analysis. The body is assumed rigid and has bounded interfaces, and the three-dimensional triangular mesh was employed. The summary of boundary conditions is shown in Table 3.

Table 3. Boundary conditions of the mechanical simulation [25]

Specification	Value	Unit
Gravity acceleration	9.80	m/s^2
Load	10	kg-f
Reference temperature	25	°C

The next simulation is the thermo-mechanical analysis. In this analysis, in addition to the mechanical and thermal loads, the internal pressure is applied to all internal faces of the radiator, aiming to provide a closer situation to the working of the car engine. The radiator is assumed fixed from the inlet and outlet locations in the simulation. The body is assumed rigid with bounded interfaces, and the three-dimensional triangular mesh is employed. Table 4 gives the values of boundary conditions.

Table 4. Boundary conditions of thermo-mechanical simulation [25]

Specification	Value	Unit
Gravity acceleration	9.80	m/s^2
Internal pressure load	1.7	MPa
Thermal load	From the previous study	-
Weigh load	10	kg-f
Reference temperature	25	°C

Then, it is intended to study the flow analysis. The related boundary conditions are according to Table 5. It is supposed that the internal liquid is water and has permanent features.

Table 5. Boundary conditions of CFD analysis [25]

#	Specification	Value	Unit
Inlet	Heat	400	k
	specified velocity (boundary normal)	1	m/s
	Particle release (Forward)	Yes	-
Outlet	Heat	300	k
	specified velocity (boundary normal)	0.83	m/s

Finally, geometrical optimization is addressed. We aim to minimize the volume of the radiator as a target, and two dimensions of the tube (10×36) are employed to find the best solution. In the next section, the results are presented.

The radiator's primary task is to lower the working temperature in the engine so that it works as well as possible. The cooler acts here as a heat exchanger when you fill the cooler with coolant. This liquid circulates around the engine with the help of an impeller that sits in the water pump and is driven by a drive belt on the engine. This causes the liquid to be heated up by the temperature in the engine and then transported to the cooler that is normally located in the front of the car. In the cooler, the liquid flows through small channels, these channels have flanges between them and it is the flanges that help with the heat exchange. With the help of either a fan, speed wind or both, the air cools down the ducts and flanges with the hot coolant and in this way the heat is led away. The cooling fan and the cooling water pump have a power consumption that is usually around 5% of the engine power [22].

Heat transfer can take place in three different ways, two of which are convection and conduction.

Convection works so that the hot and cold particles of the liquid mix and in this case the cold particles will seek out warm and cool them down and vice versa where hot particles seek out cold particles and heat them.

The cooler's primary method of heat transfer is convection, which involves heat transfer from a solid wall to a moving fluid, which in our case is the cooling fluid that is drawn around the system with the help of a pump. In the same way, we also use convection with the help of the air that flows through the cooler and cools down the outer material of the cooler, which in turn can cool the liquid on the inside. So, while the air cools the material, it also transports away heat from the liquid, which heats the material from the inside.

In this case, the convection is said to be forced because the liquid is made to flow with the help of the pump.

Water as a coolant is not optimal as there is a risk of corrosion and deposits in the engine. Therefore, desalinated water is sometimes used. However, it is most common in engines that so-called coolant is used.

The most common type of coolant is what is common-ly called glycol (ethylene glycol), but which is actually called ethanediol. Ethanediol has two tasks in the car's cooling system. The main task is to prevent frost formation in the radiator and cooling system and the secondary task is to prevent corrosion in the cooling system. Usually, the glycol is dissolved in water. The mixture consists of about 50% water and 50% glycol. This results in a freezing point of around –40 °C and a boiling point of around 108 °C. The pressure in the cooling system then raises the boiling point further, to around 120 °C.

In addition to ethylene glycol, propylene glycol is also common in cooling systems. Both are colloquially known as glycol, which makes them difficult to distinguish. It is important not to mix ethylene glycol with propylene glycol as this entails a high risk of lump formation and thus a stoppage in the cooling system. Many manufacturers color their glycols, usually red, blue or green. However, there is no industry standard for which type should have which color, which means that, for example, a blue glycol can be both ethylene glycol and propylene glycol.

Ethylene glycol is more common than propylene glycol today, as propylene glycol has somewhat poorer heat conduction and rust protection capabilities. However, ethylene glycol is very toxic. Propylene glycol is also toxic, but to a lesser extent. Drinking a small amount of ethylene glycol can be enough to cause symptoms such as unconsciousness, convulsions and severe kidney damage.

Materials: We will carry out the analysis with two different materials. Copper and an alloy with copper and aluminum. The most common material currently used in the manufacture of coolers is aluminum. But we want to compare the result with the values of a cooler made of copper as well as an alloy of these two materials to see which of the materials is preferable. Here you also have to consider the cost compared to performance in order to find out which material is the most affordable for its function. After all, the most important aspect is to be able to ensure a good function.

Temperature: Ambient temperature is set to 20 °C, which is considered the normal summer temperature in Sweden.

The temperature of the coolant is set to 120 °C, which is the liquid's boiling point, and the temperature out is set to 80 °C, which is considered reasonable.

Pressure: The pressure is set to 2.5 bar, which is overpressure for a normal cooler.

Gravity: 9.81 m/s^2.

Load from above: 250 N which corresponds to approx. 25.5 kg.

Max yield stress: 220 MPa for copper and 240 MPa for the alloy.

3. Results

In this section, based on the above-mentioned procedure for modeling, the results of FEA simulations are presented. For the thermal analysis, the displacement distribution is illustrated in Figure 4a. It is clear that the inlet tank side has more displacement and stress (1.04 mm) due to the more gradient of temperature and distance from the fixture location. Figure 4b shows the detailed displacement distribution of the upper tube of the radiator along the Y-Axis from the inlet to the outlet. It is obvious that the minimum displacement occurs when the flow is moving out of the radiator, which is around 0.15 mm. Figure 5 shows the Tresca theory's failure index. The maximum value is about 4.62, near the inlet and outlet, as expected. It results from the boundary condition simplification assumption.

For the mechanical analysis, the resulting displacement distribution is represented in Figure 6a. There is a symmetric distribution because of the symmetric geometry and loads, although it includes some simplification of the load distribution. Obviously, the maximum displacements and stresses (0.02 mm) occur far from the fixtures' location. The detailed displacement distribution of the upper tube of the radiator along the Y-Axis from the inlet to the outlet is shown in Figure 6b. Displacement has risen from the inlet to the outlet in the upper face of the tube. Figure 7 shows the Tresca theory's failure index. The maximum value is around 0.018, near the inlet and outlet as expected. It ensues from the boundary condition simplification assumption.
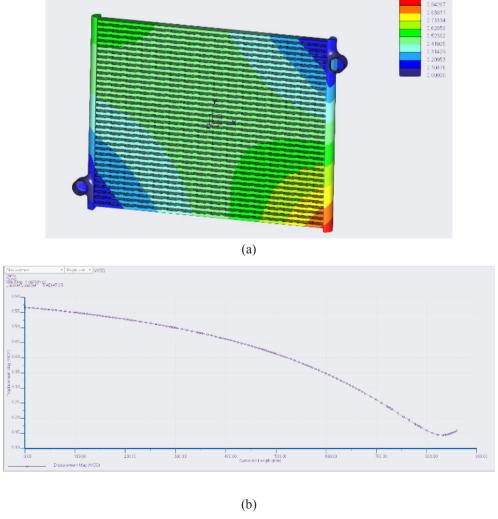

(a)

(b)

Figure 4. Resulting displacement distribution of the thermal analysis: (a) displacement distribution, (b) displacement distribution through the Y-axis1

Figure 5. Failure index distribution of the Tresca theory for the thermal analysis
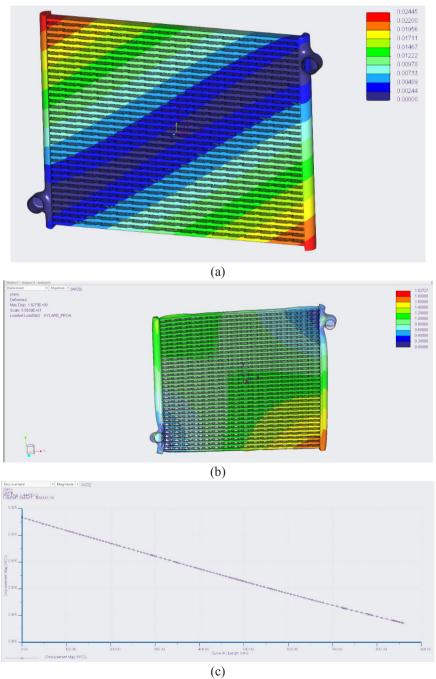

(a)

(b)

(c)

Figure 6. Resulting displacement distribution of the mechanical analysis: (a-b) displacement distribution, (c) displacement distribution through the Y-axis
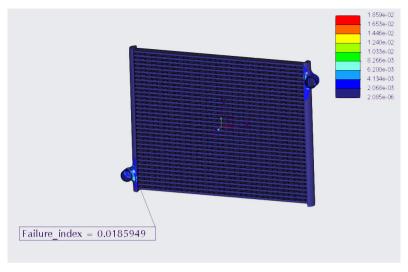
Figure7. Failure index distribution of the Tresca theory for the mechanical analysis

For the thermo-mechanical analysis, the displacement distribution is depicted in Figure 8a. There is a kind of symmetric distribution because of the symmetric geometry and mechanical loads, although thermal load causes the concentration of the stress in the inlet tank side far from the fixture location. The maximum displacement is about 1.35 mm. Figure 8b shows the detailed displacement distribution of the upper tube of the radiator along the Y-Axis from the inlet to the outlet and again from the inlet to the outlet. The displacement has risen through the upper face of the tube. Figure 9 shows the Tresca theory's failure index. The maximum value is around 4.58 happened near the inlet side as expected.
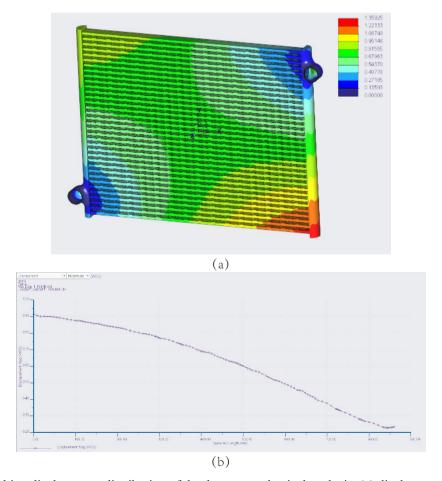

(a)

(b)

Figure 8. Resulting displacement distribution of the thermo-mechanical analysis: (a) displacement distribution, (b) displacement distribution through the Y-axis
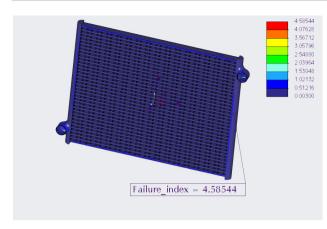
Figure 9. Failure index distribution of the Tresca theory for the thermo-mechanical analysis

Thermal stress causes seven times more displacement than a mechanical one. Although when they are combined, the value reaches 1.5 mm. It is seen that the radiator is pretty safe because in most locations, there is not any failure index of more than 1. It is clearly indicated in Figure 4a and Figure 8a that both the pure thermal and thermo-mechanical simulations have similar displacement distribution behavior. This indicates the priority of the thermal stress against the mechanical loads in the failure of the radiator. Hence, the thermal load has an important role in the failure, and it must be considered in the radiator designing process.

The results of the flow analysis are shown in Figures 10-13. Particle release starts from the inlet, and they have a forward direction into the radiator. Figure 10 illustrates velocity along X-axis. Obviously, some tubes in the middle of the radiator have lower values than others. Also, the inlet and outlet both have a medium value of velocity. In Figure 11, the internal pressure of the radiator is shown. The pressure is more in the inlet than in the outlet because they have different temperatures and conditions. Enthalpy represents the pretty harmonic distribution, as shown in Figure 12.
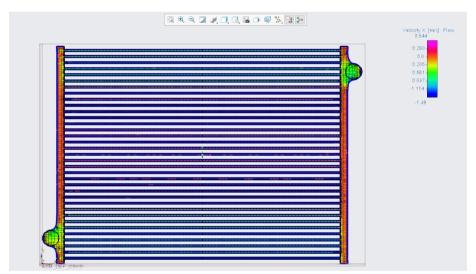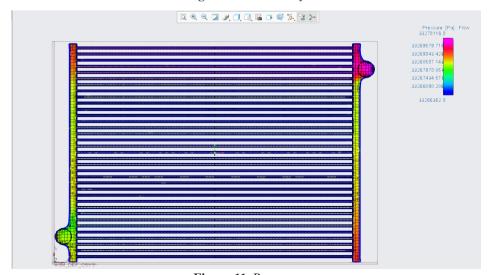

Figure 10. X-Velocity

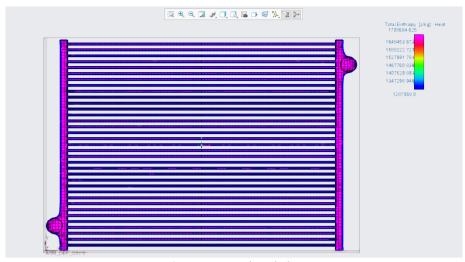**Figure 11.** Pressure
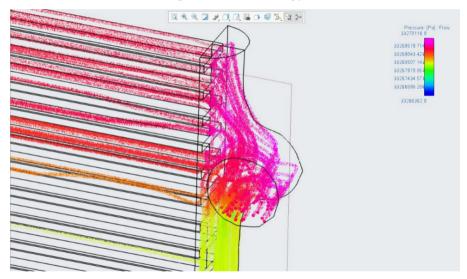
Figure 12. Total Enthalpy

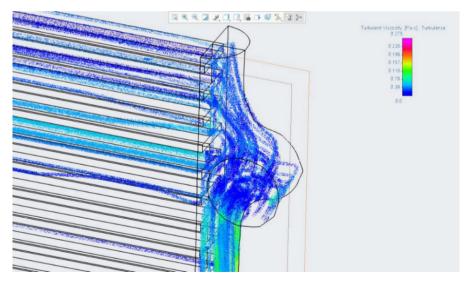**Figure 13.** The flow analysis in connection to the pressure flow

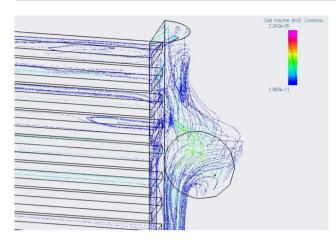**Figure 14.** The flow analysis in connection to the turbulent viscosity

Figure 15. The flow analysis in connection to the cell volume

4. Discussion

The results show that thermal stress causes 7 times more displacement than a mechanical one. Although when they have been mixed together the value grows to 1.5 mm. It is shown that the radiator is pretty safe. Because in most locations there is not any failure index of more than 1. Surprisingly results are about the effect of thermal stress and load on radiator mechanical failure.

Both pure thermal and thermo-mechanical simulation have similar displacement distribution behavior and it shows the priority of the thermal stress against mechanical loads in the failure of the radiator. So thermal load has an important role in failure and it must consider in the radiator designing process.

After carrying out the mechanical analysis (Figure 16) with regard to the failure index, it can be seen that the cooler will not make it because at certain points you see that the index is greater than 1, which corresponds to failure. What you can see is that the joints at the inlet and outlet will be extremely exposed and this is where the cooler will break.

Here we have a picture of the same analysis as the picture before, but now we have changed the material to pure copper. We see no major differences in the analysis apart from achieving a higher failure index, but the cooler will still break at the inlet and outlet respectively.

Furthermore, we also looked at displacement in mm that occurs with various loads that affect the cooler. This is by fixing an outlet which will be joined with the rest of the system in the car. Of course, the cooler will also have support in general, but these points are not included in the analysis.
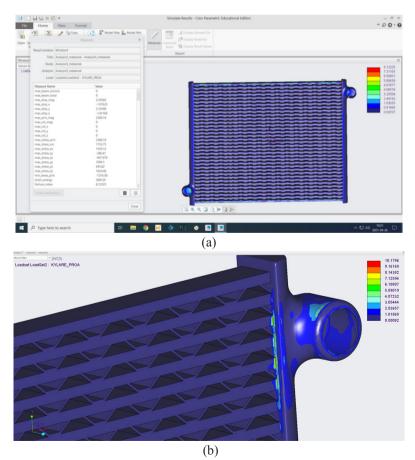

(a)

(b)

Figure 16. Mechanical analysis

In this analysis, the heat spread in the cooler is shown when the inlet temperature is 100 degrees and the outlet temperature is 80 degrees. What we readout is that it is the middle part of the cooler that is responsible for the cooling and not the edges. According to the results we got, the middle part of the radiator is 25 degrees, and this is because we could not get any liquid into the radiator. With liquid, it would have looked different as the heat in the radiator had decreased from 100 degrees down to 80 degrees instead of going from 100 to 25 and then to 80 which is not reasonable.

This analysis (Figure 17) shows how the heat affects the cooler together with the mechanical aspects. The top image shows that the shear appears to decrease when pooling the analyses. Now we only see a slightly larger impact in the lower right corner mine to displacement. Furthermore, we see that the inlet will achieve higher stress when it comes to the wrong index and ends up a bit above one, which means that the material will not hold based on the loads we put on the analysis.

4.1 Optimization of Volume

To see if an improvement to the cooler could be made, the volume of the cooler was examined. A larger volume means that a larger amount of coolant can flow through the cooling system and thus better cooling is achieved. The optimization of the volume was done with PTC Creo's analysis tool. The original volume was measured as:

$$V1 = 7747209 \text{ mm}^3 = 7.747 \text{ liters} = 0.0077 \text{ m}^3$$

After that, parameters were specified that could not be changed. Since the outer dimensions of the cooler are critical for the fit in the engine, these were specified as locked, that is, the total height and width of the cooler could not be changed. Parameters that were allowed to change were the height and width of the flanges. In the original model, the flanges were 40 mm × 10 mm (Figure 18). They were allowed to vary between 36 mm and 44 mm for the width and 9 mm and 11 mm for the height, respectively, to find the optimal volume.

The optimization resulted in the dimensions of the flanges changing from 40 mm to 44 mm in width and from 10 mm to 11 mm in height. The outer dimensions were, as previously described, locked and thus not changed. The optimization is presented in a graph where you can see how the volume is increased. The new volume was measured to:

$$V2 = 8292732 \text{ mm}^3 = 8.2927 \text{ liters} = 0.0083 \text{ m}^3$$

This means that the volume increased by $\Delta V = 545523$ mm^3 = 0.546 liters.

From the mechanical analysis carried out, we have found that the cooler's weakest link is at the inlet and outlet, where you will get high pressure. It is in these two points that deformation will mainly take place. Both at the pressure that has been applied and also at the displacement that may occur from the loads that will load the cooler.
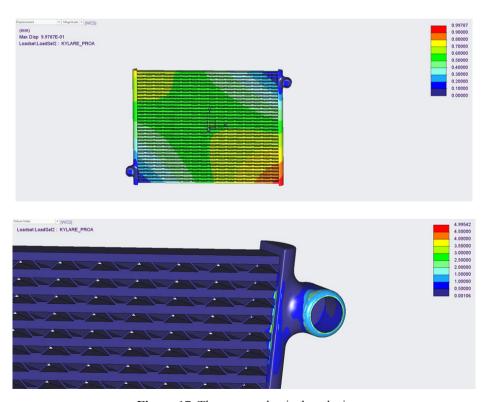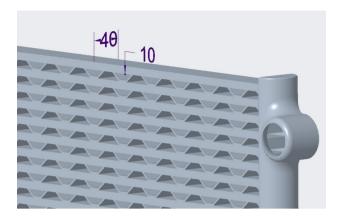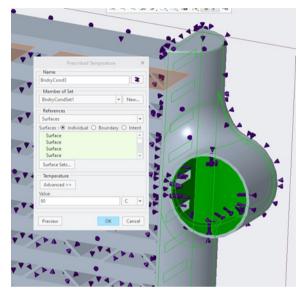

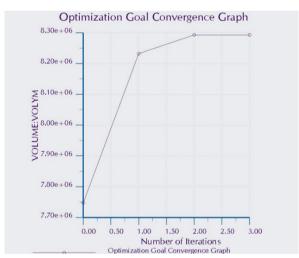**Figure 17.** Thermo-mechanical analysis

Figure 18. Graph for optimization of volume

Based on the heat analysis, the cooler will spread the heat over the entire cooler. The absolute largest part of the cooling comes from the cooling fins, as they do not have direct contact with the liquid but only cool the material around the liquid. It also appears that there is a good distribution of the heat spread in the cooler as no part stands out more than another.

The optimization resulted in the volume increasing by $\Delta V = 545523$ mm^3 = 0.546 liters.

As the volume increases, it means that we should get better cooling as more coolant can flow through the radiator. The theoretical amount of heat (the cooling effect in this case) is calculated as Q=m'*c*ΔT and the relationship between the mass flow and the volume flow is obtained from m'=ϱ * V' (Alvarez, 2006). With these two equations, we can easily see that a larger volume gives a higher volume flow, which in turn gives a larger mass flow. The greater mass flow then results in a higher theoretical cooling effect. In order to check that this is correct and how much better the cooling effect really is, a flow analysis is required, but as previously mentioned, we cannot carry that out with the student version of PTC Creo.

What we see in the heat analysis is that everything works as it should, which means that the cooler will work as it should from that point of view. We also see that it is at the heat sinks that it cools the most. If you want to optimize the cooler, you can make more but smaller cooling channels through the cooler, which all have cooling fins connected. In analysis 3, we get an unreasonable result when the heat in the cooler goes from 100 degrees to 25 and then up to 85. We got this result when the cooler only had one heat in the inlet and one heat in the outlet, this meant that the middle part of the cooler was not heated up as it should have done if you had had coolant in. The result we should have gotten would have looked like the temperature decreased exponentially as the temperature had decreased a lot at the beginning and then less at the end, until it reached the temperature.

The radiator will be deformed around the outlet and inlet because in the analysis we have fixed these points and the remaining part of the radiator which will then expose these points to the accumulated load on the radiator.

In the thermal analysis, one has gained an idea of how the radiator works regarding the cooling of the coolant when it is used during the cooling process itself. First, the liquid is hot at around 90 degrees Celsius when it flows into the inlet and then it is cooled down inside the radiator due to the fan and then it is at its coldest. When the process is finished, the radiator itself becomes warm again, but not the at same temperature as at the start.

When it comes to thermo-mechanical analysis, it's about all the safety errors within the system. Therefore, points are shown where the design was unstable and hence had more chance of being destroyed. What you see in the analysis itself is the point where there is the most chance of being destroyed when it comes to the inlet pipe where there are the most pressure & temperature increases i.e.

thermodynamic loads.

In the displacement analysis, it is the deformations that are shown that the thermodynamic loads could subject the radiator too. The maximum deformation is found at the right-bottom edge of the inlet pipe. This is obvious as it is a liquid that comes with strong pressure and high temperature which leads to the radiator's edge being deformed.

One proposed solution was to produce a gradual change when it comes to reducing the thermo-mechanical loads when discussing the inlet. This solution proposal has been tackled and managed to go through, which has led to an increase in security errors at the entrance and that is exactly what we wanted to arrive at.

The last proposed solution is the actual optimization of the flow in the radiator, where the volume is minimized by 3,962.51 square centimeters and 86 centimeters from axis to axis, in other words, the width of the radiator was shortened by 4 mm, which led to a reduction in volume. This leads to, among other things, more space for vehicles for other components. A large radiator is not always good as it is the effect itself that proves whether it is good or not.

4.2 Limitation and Future Work

There are restrictions on how Creo Simulate can establish its mathematical limit, such as restrictions on how to apply loads or constraints on merged surfaces. For instance, if the user specifies the von Mises stress value as an optimization limit (for instance, 20,000 si), Creo Simulate will seek to discover a more effective model that still satisfies both that restriction and any goal you specify by moving the model toward 20,000 psi.

The fact that this study focused more on the useful aspects of the thermal performance of the car radiator might be used to prevent the car radiator from overheating. However, due to the limited space in vehicles, relocating the heat exchanger or employing new materials may be advantageous in the development of improved heat exchangers.

4.3 Future Work

The prospective extensions of this work could be as follows:
- More simulations with transient driving cycles, improved models, and input information tailored to the individual components. This would be an appropriate technique to increase knowledge and confirm the chosen arrangement. It is also advised to do practical testing to gather pertinent information on radiators, fans, and the active cooling system.

- Additional arrangements and options might also be looked into. Condenser placement is one example.
- The incorporation of an AC system, which is not detailed in this paper, could result in even more energy and weight savings. In this situation, adding a chiller loop to enable heat pump mode ought to be looked into.
- Additionally, it is advised to use extra heat for cabin heating as necessary. Removing the LTC heater might be an option since the cabin also requires an auxiliary heater.

5. Conclusions

This study successfully performed a coupling analysis between the thermal and mechanical conditions in a typical Truck radiator. Distribution of the displacement and the failure index of Tresca theory was provided for three cases. Then, flow analyses of the radiator were investigated, including the variations of velocity, pressure, and enthalpy. The results indicate the high importance of the thermal loads necessitating their special consideration in the radiator designing process. This paper also shows the ability of PTC-Creo in the effective simulation of mechanical and thermal conditions in the radiator of a heavy-duty cooling system, which can be deemed as a reliable and economical tool for industrial applications.

When it comes to thermal analysis, it has been visualized and understood how a radiator works when it comes to cooling down the coolant in the radiator for reuse in the cooling process. The hot coolant enters the inlet where it is the hottest at 90 degrees Celsius in temperature and is slowly passed through the radiator where the heat is removed in the middle with the help of wind and a fan and there the radiator should be the coldest as shown in the analysis.

Regarding the thermo-mechanical analysis, it showed the failure safety of the whole system. It, therefore, showed which points were weakest in the design and which had the greatest risk of failure. What can be seen from the analysis is the point that has the greatest risk of failing the inlet pipe, which is understandable as it is the point that is exposed to the most thermodynamic loads such as pressure and high temperatures. The next analysis was the displacement analysis, it shows the deformation the thermodynamic loads could subject the radiator to and the maximum deformation is in the lower right corner at the inlet pipe. This is also understandable as the liquid enters with a high pressure and also a high temperature which causes the plate to deform.

In the solution proposals (Figure 19), the first thing was to make the entire plate thinner. This was done in
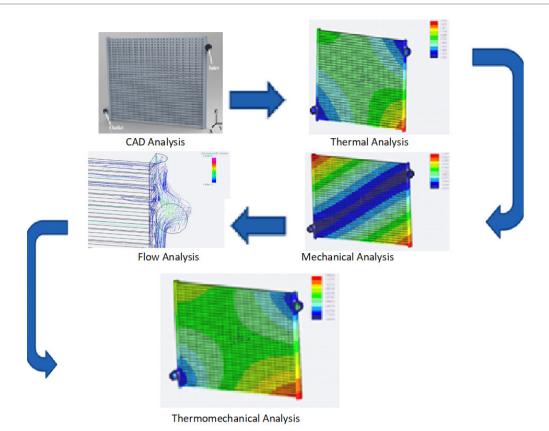
Figure 19. Graph for optimization of volume

the hope that it will be cheaper to manufacture while not too much of the strength is lost in the process. What the results of the analysis say is that it was the case, in the error safety analysis it can be seen that the error safety is not compromised too much over the whole system, there are also places like at the beginning where the error safety benefits from this improvement as it is spread out more and got better values. The displacement analysis also indicates that a thinner plate is not a bad idea as the maximum deformation of the system with the thin plate was less than the one with the thicker plate. The next solution was to create a gradual transition to reduce the thermo-mechanical loads on the entrance. The group has succeeded in this, this transition has, according to the results of the analysis, succeeded in increasing the total failure safety on the inlet pipe, which was what was the goal.

Conflict of Interest

There is no conflict of interest.

References

[1] Kasu, P.R., Ganesh, N.B., Kumar, K.S., et al., 2017. Analysis of heat dissipation in radiator of SI engine. International Research Journal of Engineering and Technology. 4, 160-166.

[2] Rahmati, A.R., Gheibi, A., 2020. Experimental and numerical analysis of a modified hot water radiator with improved performance. International Journal of Thermal Sciences. 149, 106-175.

[3] Amrutkar, P.S., Patil, S.R., 2013. Automotive radiator performance-Review. International Journal of Engineering and Advanced Technology. 2(3), 563-565.

[4] Eitel, J., Woerner, G.T., Horoho, S., et al., 1999. The aluminum radiator for heavy duty trucks. SAE Technical Paper. 1, 3727. DOI: https://doi.org/10.4271/1999-01-3721.

[5] Aravindkumar, N., Vignesh, S., Kumaran, P., et al., 2020. Computational and numerical analysis of radiator with different tube structures and nano fluid as coolant. Materials Today: Proceedings. 45(Special Issue). DOI:10.1016/j.matpr.2020.07.605.

[6] Sheikhzadeh, G., Hajilou, M., Jafarian, H., 2014. Analysis of thermal performance of a car radiator employing nanofluid. International Journal of Mechanical Engineering and Applications. 2(4), 47-51.

[7] Molana, M., 2017. On the nanofluids application in the automotive radiator to reach the enhanced thermal performance: a review. Journal of Heat and Mass Transfer. 4(4), 168-187.

[8] Abbas, F., Ali, H.M., Shah, T.R., et al., 2019. Nanofluid: Potential evaluation in automotive radiator. Journal of Molecular Liquids. 297, 112014.

[9] Sathyan, R., 2016. Analysis of automobile radiator using computational fluid dynamics. International Journal of Latest Technology in Engineering, Management & Applied Science (IJLTEMAS). 5, 6.

[10] Chidley, A., Roger, F., Traidia, A., 2011. A Thermal-Shock Fatigue Design of Automotive Heat Exchangers. International Journal of Mechanical and Mechatronics Engineering. 5(1), 263-267.

[11] Roger, F., Chidley, A., 2013. Thermo-mechanical fatigue design of automotive heat exchangers. European Journal of Computational Mechanics. 22(2-4), 228-235.

[12] Gu, J., Yang, X.F., Ma, T., et al., 2013. The study of automotive aluminum alloy radiator tank's leakage. Applied Mechanics and Materials. 364, 134-137.

[13] Baou, M., Afsharpanah, F., Delavar, M.A., 2020. Numerical study of enhancing vehicle radiator performance using different porous fin configurations and materials. Heat Transfer-Asian Research. 49(1), 502-518.

[14] Kim, T.K., Lee, S.M., Pae, S.M., 2017. Method of predicting radiator temperature distributions for thermal fatigue analysis. Journal of Mechanical Science and Technology. 31(10), 5059-5066.

[15] Amrutkar, P.S., Patil, S.R., Shilwant, S.C., 2013. Automotive radiator-design and experimental validation. Research and Development (IJAuERD). 3(4), 1-10.

[16] Shariff, K.B., Abdullahi, B., Abubakar, S.B., 2018. Modelling and simulation of car radiator: Effects of fins under the atmospheric condition of Kano, Nigeria. Journal of Advanced Research in Fluid Mechanics and Thermal Sciences. 48(1), 1-16.

[17] Mia, S., Hossen, S., 2019. Numerical observation of heat transfer and pressure behaviour in an automobile radiator. Journal of Mechanical Engineering. 49(2).

[18] Patel, H.V., Subhedar, D.G., Ramani, B., 2017. Numerical investigation of performance for car radiator oval tube. Materials Today: Proceedings. 4(9), 9384-9389.

[19] Kasu, P.R., Ganesh, N.B., Kumar, K.S., et al., 2017. Analysis of heat dissipation in radiator of SI engine. International Research Journal of Engineering and Technology. 4, 160-166.

[20] Bonato, M., 2020. From Manufacturing Process Control to In-Field Reliability: Case Study of Automotive Heat Exchangers [Internet]. 2020 Annual Reliability and Maintainability Symposium (RAMS) [Published 2020 January 27]. pp. 1-7. Available from: https://dl.acm.org/doi/10.1109/RAMS48030.2020.9153724.

[21] Goyal, N., Kaushik, A., Ram, M., 2016. Automotive water cooling system analysis subject to time dependence and failure issues. International Journal of Manufacturing, Materials, and Mechanical Engineering (IJMMME). 6(2), 1-22.

[22] Henrik, A., 2006. Energiteknik Edition. pp. 360-370. ISBN: 9789144045092.

[23] Tenkel, F.G., 1974. Computer Simulation of Automotive Cooling Systems. SAE Technical Paper. 2, 1. DOI: https://doi.org/10.4271/740087.

[24] Global Auto Parts & Accessories Marketplace [Internet]. SCANIA Radiator 1365371. Available from: http://bonamotor.en.gasgoo.com/auto-products/1450301.html.

[25] Aluminium Matter Organization UK. [Interner]. Available from: https://european-aluminium.eu/.

[26] Ellis, D.E., 1960. Mechanical properties of aluminum alloys at various temperatures. Atomics International. Div. of North American Aviation, Inc., Canoga Park. United States: N. Available from: https://www.osti.gov/biblio/4097760.

[27] Peyghambarzadeh, S.M., Hashemabadi, S.H., Naraki, M., et al., 2013. Experimental study of overall heat transfer coefficient in the application of dilute nano fluids in the car radiator. Applied Thermal Engineering. 52(1), 8-16.

ARTICLE

Thermo-Mechanical Modeling of High-Strength Concrete Column Subjected to Moderate Case Heating Scenario in a Fire

Tarek Eltalhi[1]   Awad S. Bodalal[1]   Farag M. Shuaeib[1]   Vail Karakale[2*]

1. Mechanical Engineering Department, Faculty of Engineering, University of Benghazi, Benghazi, 00218, Libya
2. Civil Engineering Department, Faculty of Engineering and Natural Sciences, Istanbul Medeniyet University, Istanbul, 90212, Turkey

ABSTRACT

This paper presents a numerically developed computer model to simulate the thermal behavior and evaluate the mechanical performance of a fixed ends centrically loaded High Strength Concrete Column (HSCC), subjected to Moderate Case Heating Scenario (MCHS), in a hydrocarbon fire. The temperature distribution within the mid-height cross-sectional area of the column was obtained to determine the thermal and mechanical responses as a function of temperature. The governing two-dimensional transient heat transfer partial differential equation (PDE), was converted into a set of ordinary algebraic equations, subsequently, integrated numerically by using the explicit finite difference method, (FDM). A computer program, Visual Basic for Applications (VBA), was then developed to solve the set of ordinary algebraic equations by implementing the boundary as well as initial conditions. The predictions of the model were validated against experimental data from previous studies. The general behavior of the model as well as the effect of the key model parameters were investigated at length in the review. Finally, the reduction in the column's compression strength and the modulus of elasticity was estimated using correlations from existing literature. And the HSCC failure load under fire conditions was predicted using the Rankine formula. The results showed that the model predictions of the temperature distribution within the concrete column are in good agreement with the experimental data. Furthermore, the increase in temperature of the reinforced concrete column, (RCC), due to fire resulted in a significant reduction in the column compression strength and considerably accelerates the column fire failure load.

1. Introduction

Naturally or intentionally, fire is a catastrophic disaster. When it is set, invariably a vast number of losses in both property and lives are expected. As an eyewitness, we have seen huge damage in buildings as a result of

---

*Corresponding Author:
Vail Karakale,
Civil Engineering Department, Faculty of Engineering and Natural Sciences, Istanbul Medeniyet University, Istanbul, Turkey;
Email: vail.karakale@medeniyet.edu.tr

the progression use of fire weapons during the Libyan civil war in 2011. On the other hand, the efforts of developing simulation models of fire effects on building's structural members will never stop saving people's lives and their properties.

When a building catches fire, the structural integrity and stability are dependent on the column's ability to resist failure at elevated temperatures, which is the first and last line of defense to maintain the column's strength. As a primary load-bearing member, the column is designed to withstand axial centric and/or eccentric loads of any structure. In other words, it carries the whole building's live and dead loads.

According to the related international standard codes, the fire resistance of any structural member is obtained experimentally. This is an expensive and time-consuming procedure and the utility of published experimental test data in a practical engineering design exercise is questionable. Although experimental studies are decisive, and the outcome is limited to the number of measurements taken during the test, experimental data can be used in the calibration and validity of the mathematical and numerical models, as mentioned in many studies [1-6].

While numerical simulation models generate much more useful interpretable data, there is a limit to which experimental tests can be conducted. Recently, emphasis is placed on mathematical simulation models to replace the existing experimental fire rating-based design methods with performance-based design procedures. Generally, concrete structural exhibits good performance under normal situations. However, results from several studies have shown that there are well-defined differences between the properties of high-strength concrete and normal-strength concrete during a fire since the former is much more durable and stronger than the latter. Furthermore, concerns have been developed regarding the reduction in strength of high-strength concrete when subjected to elevated temperature [7-13].

The main objective of this study is to develop a 2D numerical simulation basic computer model to predict the thermal behavior, to evaluate the mechanical performance of preloaded HSCC, and to set the failure criteria of the such column in a standard fire. The model development will be conducted by following the rule of elimination of some variables and parameters, and refining the code by neglecting non-significant parameters, assuming values for other factors, and using correlations and expressions from previous related studies to predict temperature distribution and strength profiles within the selected quarter cross-section area of the subjected HSCC.

1.1 Behavior of HSC Exposed to Fire

The fire-resistance rating of a concrete structural member is a function of applied load intensity and centricity, member type (e.g., column or beam or wall), member dimensions and boundary end conditions, incident heat flux from the fire on the member or assembly, type of construction materials (e.g., concrete, steel & wood) and finally, the effect of temperature rise within structural member on relevant properties of the member. The concrete is classified as Normal Strength Concrete (NSC), with a compressive strength of < 70 MPa, and High Strength Concrete (HSC) with a compressive strength of ≥ 70 MPa [14-17].

The use of HSC is widely increasing recently especially in High-rise buildings, offshore structures, and bridges because it has higher strength and improved durability compared to NSC, but in the fire incident, NSC performs better than HSC due to its low permeability which reduces the effect of spalling in fire [17], as shown in Figures 1a and 1b.

a

b

Figure 1. a) NSCC in a fire exposure test; b) HSCC in a fire exposure test

Data from the experimental research that was carried out at specialized laboratories, as well as some worldwide organizations show that concentrically loaded and short

columns failed in pure compression while eccentrically loaded and long columns failed in combined flexure/compression mode due to buckling spalling [2,11-13]. Figures 2a and 2b for example show the effect of one of those factors namely the effect of the lateral reinforcement configuration on the spalling behavior in HSC Columns after the fire resistance test [17].

a

b

Figure 2. a) Conventional tie configuration; b) Modified tie configuration

1.2 The Effect of High Temperature on Steel Reinforced Concrete Structural Member

The fire performance of any structural member depends on the thermal and mechanical properties of the materials from which the building component is made. The critical temperature of fully-loaded structural member building materials such as steel and concrete is defined as the temperature at which the integrity of the member lost 50% of its original yield strength at 20 °C and becomes questionable. The building code requirements for structural fire protection are based on tests conducted following ASTM E-119. In these tests, the performance criteria for building assemblies, such as columns, is the loading bearing capacity, when these assemblies are exposed to heating conditions the mechanical properties that affect the fire performance of the structural members such as Compression Strength, Modulus of elasticity, Coefficient of thermal expansion, and Creep [4,18].

In the case of slender columns, the susceptibility for buckling increases with a decrease in the modulus of elasticity, and the concrete modulus of elasticity decreases rapidly with the rise of temperature. If steel reinforcement attains a temperature of 550 °C the modulus of elasticity is reduced to approximately half of the value at ambient and the concrete strength decrease is minimal up to about 300 °C, above these temperatures, the concrete strength loss is significant [12].

Steel-reinforced concrete columns are designed to withstand the applied load, although concrete will carry more load than steel, both will share the load in normal conditions [3]. When a column made of two different materials is subjected to fire under a given axial load at a certain temperature, one of those materials will carry the total load because of the thermal expansion differences, as there is no relative movement between concrete and steel in the reinforced concrete unit, elongation or contraction of both concrete and steel will be the same, equally strained before failure occurrence [18].

2. Materials and Methods

The thermal modeling that is used in this paper is based on the ASTM E-119 standard fire curve as shown in Figure 3 which describes the hydrocarbon fire development [2,17,19].

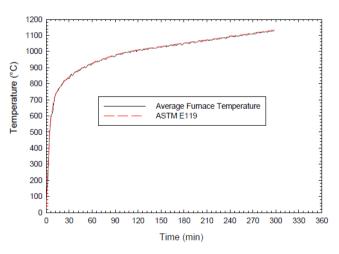**Figure 3.** ASTM E-119 Standard temperature VS time

$$T(t) = T_0 + 750 \times \left(1 - e^{-3.79533\sqrt{t}}\right) + 170.4 \times \sqrt{t} \quad (1)$$

where, t = time in hours, and T_0 = 20 °C, initial temperature used as boundary condition in both x and y directions.

2.1 Model Development

The physical description and cross-sectional configuration of the subjected HSCC which is surrounded by air with time-changing temperature according to E-119 are shown in Figures 4a and 4b.
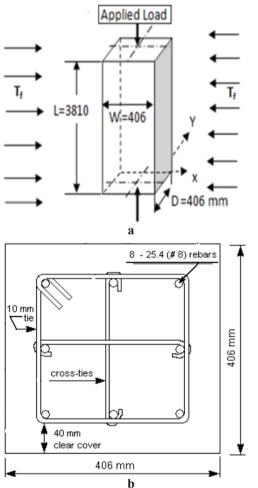

Figure 4. a) Physical description of the model; b) HSCC cross-sectional configuration

2.2 Equations and Key Assumptions

Basically, the heart of the model is the variable thermal boundary conditioned with the famous two-dimensional transient conduction heat transfer equation with constant thermal properties (Equation 2):

$$k\frac{\partial}{\partial x}\left[\frac{\partial T}{\partial x}\right] + k\frac{\partial}{\partial y}\left[\frac{\partial T}{\partial y}\right] + q = \rho c_p \frac{\partial T}{\partial t} \qquad (2)$$

Divide both sides by k, neglecting heat generation inside the column $q = 0$, and replace [$k / (\rho c_p)$] with thermal diffusivity (α), we get:

$$\frac{\partial^2 T}{\partial x^2} + \frac{\partial^2 T}{\partial y^2} = \frac{1}{\alpha}\frac{\partial T}{\partial t} \qquad (3)$$

Then the central finite difference expression is used to approximate the partial differential second-order terms. Hence, a set of first-order Ordinary Differential Equations (ODE's) resulted.

2.3 Computation Domains and Solution Techniques

The first step in the formulation is to subdivide the x and y directions into equally spaced nodes. For the sake of numerical stability, the computational domain is divided into (W/2 = D/2 = 203 nodes) in each direction. To implement the boundary conditions the fire-exposed surfaces and symmetry lines nodes are formulated differently from the rest of the interior nodes.

Finally, the resulting set of (ODE's) is solved by using the explicit finite difference method and the 2-D transient temperature distributions within the concrete column is founded.

The two-dimensional transient conduction heat transfer configuration for the interior nodes according to FD numerical method procedure is shown in Figure 5.

$$\frac{\partial^2 T}{\partial x^2} = \frac{\left[T_{(m-1, n)}^P + T_{(m+1, n)}^P - 2T_{(m, n)}^P\right]}{\Delta x^2} \qquad (4)$$

$$\frac{\partial^2 T}{\partial y^2} = \frac{\left[T_{(m, n-1)}^P + T_{(m, n+1)}^P - 2T_{(m, n)}^P\right]}{\Delta y^2} \qquad (5)$$

$$\frac{\partial T}{\partial t} = \frac{\left[T_{(m, n)}^{P+1} - T_{(m, n)}^P\right]}{\Delta t} \qquad (6)$$

Figure 5. Interior nodes configuration
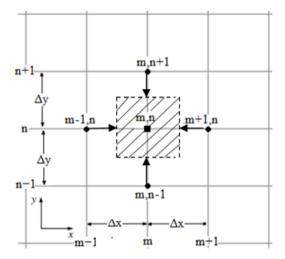
Substituting Equations (4), (5) & (6) into Equation (3), we get the governing two-dimensional transient conduction heat transfer equation for interior nodes:

$$T_{m,n}^{P+1} = F_o\left(T_{m-1,n}^P + T_{m+1,n}^P + T_{m,n-1}^P + T_{m,n+1}^P\right) + (1 - 4F_o)T_{m,n}^P \qquad (7)$$

where, $\Delta x = \Delta y = \Delta s$ (Equally spacing). $F_o = \alpha \times \Delta t / \Delta s^2$,

Fourier number dimensionless parameter.

The stability criteria of Equation (7) are maintained as long as ($F_o \leq 0.25$) or ($\alpha_i \leq 2.5 \times 10^{-7}$ m^2/sec).

According to Kumar [20], in a moderate case heating scenario, MCHS, where the effect of linear convection and radiation is combined into an equivalent non-linear convection term:

$$h\,(T_f + T_s)^N = h(T_f + T_s) + \varepsilon\,\sigma\big(\overline{T_f^4} + \overline{T_{fs}^4}\big) \tag{8}$$

The mild exposure principle from the literature [20], MCHS, is adopted to determine the column expose surface temperature, T_s.

Figure 6 shows that the corner surface fire exposed node is subjected to convection, radiation from the bottom and left-hand sides, and conduction from the top and right sides.

Combined equivalent (Convection and Radiation) term + Conduction term = $\rho C_p \dfrac{\partial T}{\partial t}$ Transient term
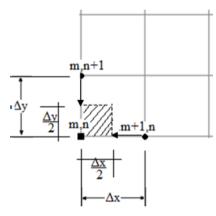

Figure 6. Corner surface node configuration.

$$T_{m,n}^{P+1} = \frac{2\,\Delta t\,\alpha}{\Delta s^2}\left[\frac{2\,\Delta s\,h_f}{K}\big(T_f^P - T_{m,n}^P\big)^N + \big(T_{m+1,n}^P + T_{m,n+1}^P\big)\right] + \left(1 - \frac{4\,\Delta t\,\alpha}{\Delta s^2}\right)T_{m,n}^P \tag{9}$$

Figure 7 shows that the bottom surface fire exposed node is subjected to convection and radiation from the bottom side and conduction from the top, right and left sides.
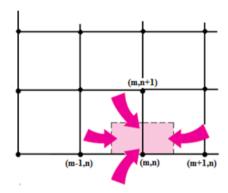

Figure 7. Bottom surface node configuration.

$$T_{m,n}^{P+1} = \frac{\Delta t\,\alpha}{\Delta s^2}\left[\frac{2\,\Delta s\,h_f}{K}\big(T_f^P - T_{m,n}^P\big)^N + \big(T_{m-1,n}^P + T_{m+1,n}^P\big) + 2T_{m,n+1}^P\right] + \left(1 - \frac{4\,\Delta t\,\alpha}{\Delta s^2}\right)T_{m,n}^P \tag{10}$$

Figure 8 shows that the side surface fire exposed node is subjected to convection and radiation from the left-hand side and conduction from the top, right and bottom sides.
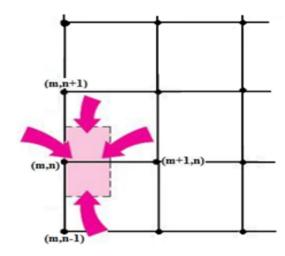

Figure 8. Side surface node configuration.

$$T_{m,n}^{P+1} = \frac{\Delta t\,\alpha}{\Delta s^2}\left[\frac{2\,\Delta s\,h_f}{K}\big(T_f^P - T_{m,n}^P\big)^N + \big(T_{m,n-1}^P + T_{m,n+1}^P\big) + 2T_{m+1,n}^P\right] + \left(1 - \frac{4\,\Delta t\,\alpha}{\Delta s^2}\right)T_{m,n}^P \tag{11}$$

Kumar [20] proposed the simplest form of thermal diffusivity as a function of temperature:

$$\alpha_t = \frac{1.45}{(T+400)}, \quad \text{m}^2/\text{hr} \tag{12}$$

Initial, t = 0 and temperature $T_i = 20\ °C$. Therefore, $\alpha_T = 9.58 \times 10^{-7}$ m^2/sec, consequently this value violates the stability criteria of the adopted FD numerical method to solve Equation (7). Hence, the constants 1.45 and 400 in Equation (12) will be examined and refined to suit the thermal analysis and minimize the difference between experimental data and the thermal simulation model output.

2.4 Boundary and Initial Conditions

The reinforcement steel bars will be neglected in the thermal analysis, because they represent only 2.45% of the gross cross-sectional area of the column. Hence the material of the column was considered wholly concrete as homogenous in the thermal branch.

The subjected HSCC cross-sectional area at the mid-height is divided into four segments by two symmetry lines (double symmetric shape), only a quarter of the section is analyzed. It was equally spaced into a sufficient number of nodes, $\Delta x = \Delta y$ each representing a square millimeter of the column's cross-sectional area, with two

perpendicular hot air-surrounded surfaces and the other two perpendicular surfaces representing the boundary symmetry lines.

There are four boundary conditions at the *x* and *y* directions (two at the fire-exposed surfaces and two at the symmetry lines) and one initial condition at τ= 0. These are:

$$T (x, y, 0) = T_i = 20 \,°C \quad, \quad T (x, 0, t) = T_s (x, 0, t) \quad,$$
$$T (0, y, t) = T_s (0, y, t)$$

$$T(W/2, \, y, t) = \frac{[T(x_{m+1}, y, t) + T(x_{m-1}, y, t)]}{2}$$

$$T(x, D/2, t) = \frac{[T(x, y_{n+1}, t) + T(x, y_{n-1}, t)]}{2}$$

After that, the model will be ready for another step forward, in other words; correlations of remaining strengths for both steel reinforcement and concrete from the existing literature will be introduced to determine the strength reduction of both materials during the fire exposure scenario.

Muhammad Yaqub et al. [18], proposed the following correlations (13) and (14) to measure the effect of elevated temperature on the HSCC strength for both concrete and reinforcement bars.

To calculate the steel bars remaining strength:

$$\xi_{st} = \kappa + \frac{1-\kappa}{1+\left(\frac{T}{T_1}\right)+\left(\frac{T}{T_2}\right)^2+\left(\frac{T}{T_8}\right)^8+\left(\frac{T}{T_{64}}\right)^{64}} \tag{13}$$

where, ξ_{st} is the ratio between the remaining compressive strength at temperature T °C and the original unheated compressive strength of reinforcing steel bars at 20 °C. κ, T_1, T_2, T_8, and T_{64}, are given tabulated parameters for various types of steel.

To calculate the concrete remaining strength:

$$\xi_c = \frac{1}{1+\left(\frac{T}{T_1}\right)+\left(\frac{T}{T_2}\right)^2+\left(\frac{T}{T_8}\right)^8+\left(\frac{T}{T_{64}}\right)^{64}} \tag{14}$$

where, ξ_c is the ratio between the remaining compressive strength at temperature T °C and the original unheated compressive strength of concrete at 20 °C. T_1, T_2, T_8, and T_{64}, are given tabulated parameters for various types of aggregates.

The types of steel most often used in building design and construction is either hot-rolled or cold-drawn, with a modulus of elasticity of about 210 GPa at 20 °C [12-14].

The specifications of steel bars 400 MPa compression yield strength (25 mm diameter), from literature by Kodur et al. [17] were used to evaluate the performance of HSCC in a fire.

As shown in Table 1, Euro-code classified HSC into three classes, depending on its Cylinder / Cube compressive strength [12]:

Table 1. HSC Euro-code classifications

Classification	Minimum GPa	Maximum GPa
Class 1	55 / 67	60 / 75
Class 2	70 / 85	80 / 95
Class 3	90 / 105	Higher

The effects of temperature on the elastic modulus of concrete and the reinforcing bars are proposed in the literature [21]. Equation (15) showed the ratio of the reinforcing bars' modulus of elasticity at elevated temperature to the reinforcing bars' modulus of elasticity at room temperature.

$$\frac{E_{st,T}}{E_{st,20\,C^0}} = \begin{cases} 1 + \frac{T}{\left[2000 \times \ln\left(\frac{T}{1100}\right)\right]}, & for\ 0°C < T \le 600°C \\ 690 \times \frac{\left(1-\frac{T}{1000}\right)}{(T-53.5)}, & for\ 600°C < T \le 1000°C \end{cases} \tag{15}$$

The modulus of elasticity of concrete also decreases as temperature increases [21]. Equation (16) showed the reduction ratio of concrete modulus of elasticity due to temperature increase.

$$\frac{E_{c,T}}{E_{c,20\,C^0}} = \begin{cases} 1, & for\ T < 150°C \\ \frac{(700-T)}{550}, & for\ T \ge 150°C \end{cases} \tag{16}$$

The concrete modulus of elasticity at room temperature may fall within a very wide range, 5 to 50 GPa.

Table 2, shows reinforced concrete elasticity moduli at room temperature based on the type of aggregate of the reinforced concrete [12-14]:

Table 2. Concrete Modulus of elasticity at 20 °C

Type of aggregate	Modulus of elasticity $E_{C, 20 °C}$
Carbonate aggregate	34 GPa
Silicate aggregate	38 GPa
Light weight aggregate	19 GPa

Kang Hai Tan [3] proposed the Rankine formula correlations, Equations (17) to (19), to predict the failure load of the reinforced concrete column under fire conditions.

$$\frac{1}{P_{R(t)}} = \frac{1}{u_{pr} \times P_{p(t)}} + \frac{1}{P_{e(t)}} \tag{17}$$

$$P_{p(t)} = \beta_{c(t)}\, f'_{c(0)}\, A_C + \beta_{yr(t)}\, f_{y(0)}\, A_{st} \tag{18}$$

$$P_{e(t)} = \frac{\pi^2 [\beta_{Ec(t)}\, 0.2\, E_{c(0)}\, I_c + \beta_{Est(t)}\, E_{sr(0)}\, I_{st}]}{L_e^2} \tag{19}$$

where,

$P_{R(t)}$: Predicted failure load by Rankine formula.

$P_{p(t)}$: Plastic squashing load of RCC at time **t**.

$P_{e(t)}$: Elastic buckling load of RCC at time **t**.

.t: Fire exposure time.

A_c: Column concrete cross-section area.

A_{st}: Column reinforcing steel cross-section area.

$.f_c'$: Concrete cylinder compression strength.

f_y: Steel reinforcement yield strength.

E_c: Concrete elastic modulus.

E_{st}: Steel reinforcement elastic modulus.

I_c: Concrete 2nd moment of area.

I_{st}: Steel reinforcement 2nd moment of area.

L_e: Column effective length.

$.c$: Column concrete covering in mm.

Concert strength reduction factor in fire:

$$\beta_{c(t)} = \frac{\gamma_{(t_e)}}{\sqrt{1+\left(0.3\,A_c^{-0.5}\,t_e\right)^{A_c^{-0.25}}}} \qquad (20)$$

Steel strength reduction factor in fire:

$$\beta_{yr(t)} = \gamma_{(t_e)}\left(1 - \frac{0.9\,t_e}{0.046\,c+0.11}\right) \geq 0 \qquad (21)$$

$$\gamma_{(t_e)} = 1 - 0.3\,t_e \geq 0.85, \quad t_e = \alpha_{agg} \times \alpha_{ISO} \times t \qquad (22)$$

$$\alpha_{agg} = \left\{ \begin{array}{c} 1 \text{ for siliceous aggregate} \\ 0.9 \text{ for carbonate aggregate} \end{array} \right\}, \text{ and}$$

$$\alpha_{ISO} = \left\{ \begin{array}{c} 1 \text{ for ISO 834 Standard fire} \\ 0.85 \text{ for ASTM} - \text{E119 Standard fire} \end{array} \right\} \qquad (23)$$

2.5 Model Flow Chart

Figure 9 shows the model flow chart of the numerical thermal simulation and mechanical performance evaluation of the subjected HSCC based on the adopted MCHS in a fire.
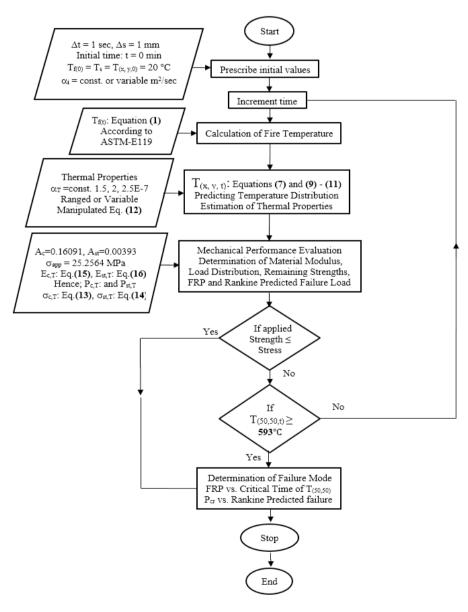

Figure 9. Flow chart of the MCHS numerical simulation model

3. Results

The main findings of this study are presented in this section. They are laid out in three main subsections. The thermal simulation (temperature distribution) and model prediction validation, statistical error analysis for testing the model prediction accuracy, and the mechanical performance evaluation of the subjected HSCC fire response characteristics of constituent.

3.1 General Behavior of the Model

In the first subsection, the temperature distribution in the cross-sectional area at mid-height of the subjected HSCC is determined according to the adopted MCHS with constant, ranged, and variable thermal diffusivities in a fire. The temperature distribution at different depths is validated by experimental data from the literature.

Figure 10a shows the temperature distribution in MCHS with constant concrete thermal properties: $\alpha = 2.5 \times 10^{-7}$ m^2/sec, k = 1.5 W/(m-^{o}C), combined heat transfer coefficient: h_f = 15 W/(m^2-^{o}C), and combined heat transfer exponent: N = 1.55.

One observation that can be made is that as the time interval increases, so does the temperature of the concrete column. Logically, this is because as more time passes, a greater quantity of heat would enter the column thus elevating its temperature.

Figure 10b shows that the thermal diffusivity ($\alpha = 2.5 \times 10^{-7}$ m^2/sec) is suitable for predicting the temperature distribution of nodes at 76 mm depth only, overestimates temperature for nodes at 13, 32, and 50 mm depths, and underestimates temperature for nodes deeper than 76 mm.
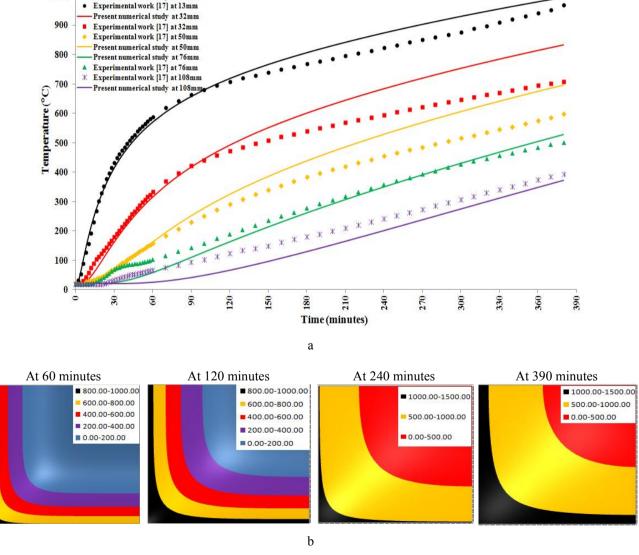

a

b

Figure 10. a) MCHS Temperature distribution with $\alpha = 2.5 \times 10^{-7}$ m^2/sec at 13, 32, 50, and 76 mm depths VS time and against the related previous experimental test results. b) Temperature contour of MCHS with 2.5×10^{-7} m^2/sec thermal diffusivity.

Figures 11a and 11b show temperature distribution and contour in MCHS with constant concrete thermal properties: $\alpha = 2.0 \times 10^{-7}$ m²/sec, k = 1.5 W/(m-°C), combined heat transfer coefficient: $h_f = 15$ W/(m²-°C), and combined heat transfer exponent: N = 1.55.

Figure 11a shows that the thermal diffusivity ($\alpha = 2.0 \times 10^{-7}$ m²/sec) is suitable for predicting the temperature distribution of nodes at 50 mm depth only, overestimates temperature at 13, and 32 mm, and underestimates temperature for nodes deeper than 50 mm.

Figures 12a and 12b show temperature distribution and contour in MCHS with constant concrete thermal properties: $\alpha = 1.5 \times 10^{-7}$ m²/sec, k = 1.5 W/(m-°C), combined heat transfer coefficient: $h_f = 15$ W/(m²-°C), and combined

heat transfer exponent: N = 1.55.

Figure 12a shows that the thermal diffusivity ($\alpha = 1.5 \times 10^{-7}$ m²/sec) is suitable for predicting the temperature distribution of nodes at 13, and 32 mm depths after 180 minutes of fire exposure only, and underestimates temperature for all nodes at all times. (Lower value of thermal diffusivity is more suitable particularly for the closer nodes to the fire-exposed surfaces and vice versa).

The fluctuation of nodal temperatures with the change of thermal diffusivity during the increase of fire temperature is solid evidence that led to the first conclusion which confirms that the material properties are not constants but functions of temperatures, depths and fire time.
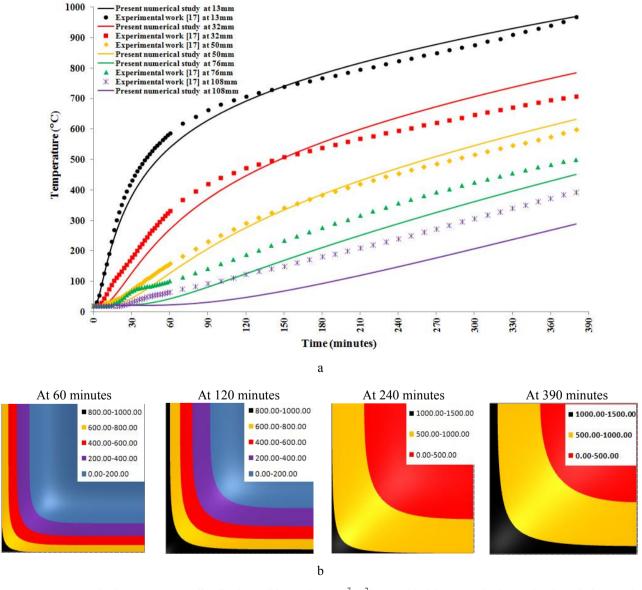

a

b

Figure 11. a) MCHS Temperature distribution with $\alpha = 2.0 \times 10^{-7}$ m²/sec at 13, 32, 50, and 76 mm depths VS time and against the related previous experimental test results. b) Temperature contour of MCHS with 2.0×10^{-7} m²/sec thermal diffusivity.
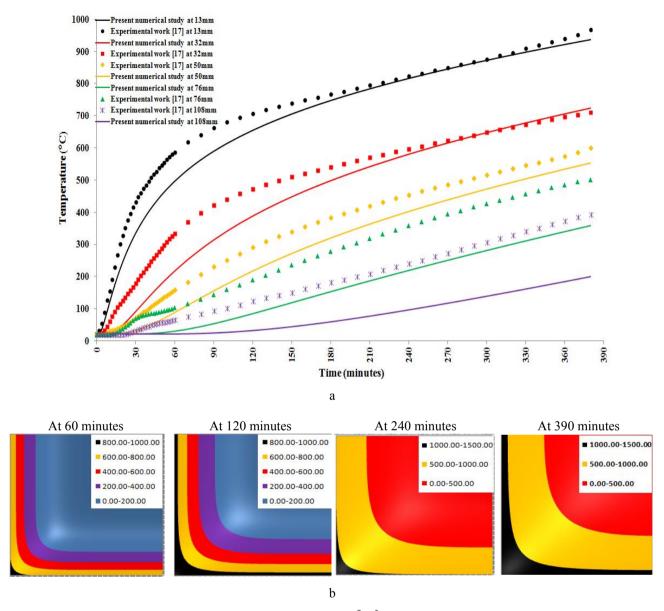
a

b

Figure 12. a) MCHS Temperature distribution with $\alpha = 1.5 \times 10^{-7}$ m^2/sec at 13, 32, 50, and 76mm depths VS time and against the related previous experimental test results. b) Temperature contour of MCHS with 1.5×10^{-7} m^2/sec thermal diffusivity.

Constants in the proposed correlation of thermal diffusivity [12], Equation (12), were examined and manipulated to form a function of temperature and time that suit the thermal temperature distribution and minimizes the difference between experimental data and numerical model output.

$$\alpha_{i,j,t} = A \times \frac{e^{\left(-B \times \text{time}\right)}}{\left(3600 \times (T + 400)\right)},$$

where;
A: $0.75 - 0.875$
B: $0.0006 - 0.0001$

For spacing ranges
0 – 16 mm
20 – 36 mm
40 – 56 mm
60 – 76 mm
80 – 96 mm
100 – 203 mm

Figure 13a shows that the model temperature distribution output is improved when introducing the thermal diffusivity as a function of temperature and time that varies for each layer of depth.

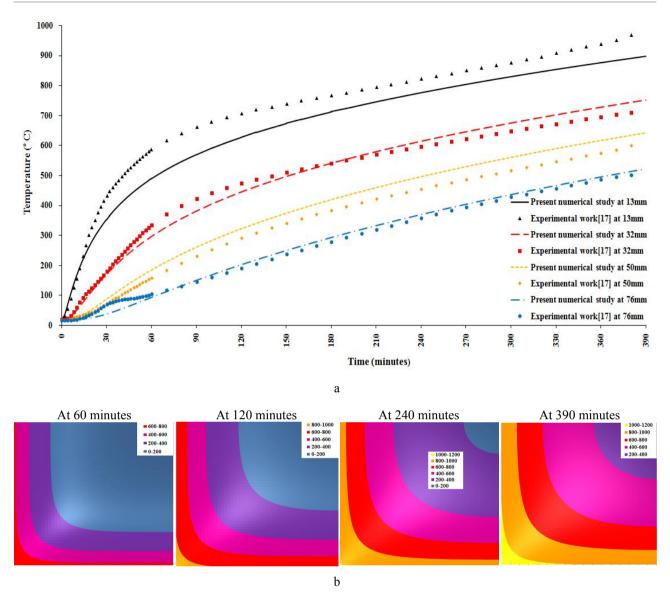The resulting manipulated correlation of the ranged

41

a

b

Figure 13. a) MCHS Temperature distribution with ranged thermal diffusivity at 13, 32, 50, and 76 mm depths VS time and against the related previous experimental test results. b) Temperature contour of MCHS with ranged thermal diffusivity.

thermal diffusivity that generates temperature distribution in Figure 13a was refined to be a function of temperature, time, and depth, in other words a correlation for all layers instead of one correlation for each layer of depth.

$$\alpha_{i,j,t} = 0.01 \sqrt{(x^2 + y^2)} \frac{e^{(-0.1 \times time/60)}}{\left(3600 \times \left(T_{i,j,t} + 400\right)\right)}, \quad m^2/Sec.$$

where; $\begin{cases} x_i \text{ and } y_j \text{ in mm} \\ \text{time in minutes} \\ T \text{ in } °C \end{cases}$

Figure 14a shows that the temperature distribution accuracy was not fully improved by using the variable thermal diffusivity compared with Figure 13a which showed

the temperature distribution when introducing the ranged thermal diffusivity.

Figures 10a, 11a, 12a, 13a, and 14a show the resulted model temperature distribution when using constant ((1.5, 2.0, and 2.5)×10⁻⁷), ranged, and variable thermal diffusivities (m²/sec), they also show that the validation of model output results for every case by comparing the model predictions with the related previous experimental data from the literature.

3.2 Test Model Prediction Accuracy

In the second subsection, the model predictions accuracy is tested by conducting a statistical error analysis
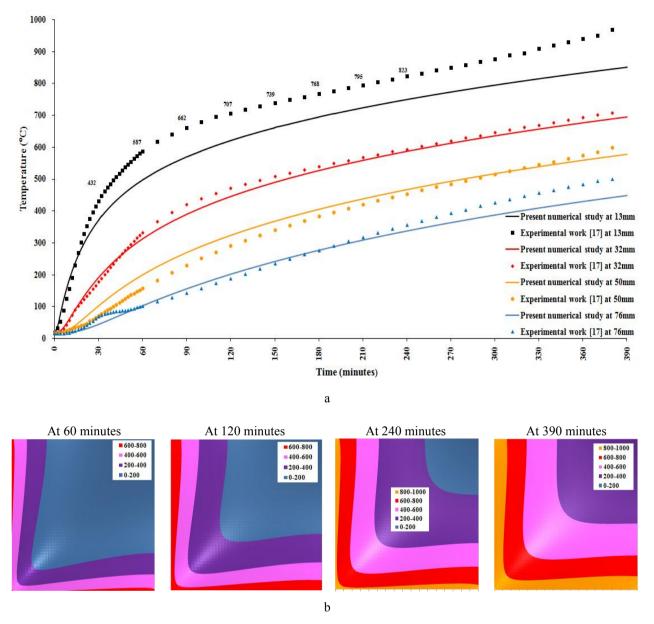
a

b

Figure 14. a) MCHS Temperature distribution with variable thermal diffusivity at 13, 32, 50, and 76mm depths VS time and against the related previous experimental test results. b) Temperature contour of MCHS with variable thermal diffusivity.

including:

1) Mean percentage error, (MPE), provides information on the mean percentage error of the predicted readings about the actual reading or experimental data [22].

$$MPE = \left\{ \sum \left[\frac{(T_{exp} - T_t)}{T_{exp}} \times 100 \right] \right\}/n$$

2) Mean bias error, (MBE), provides information with respect to overestimation or underestimation (A low MBE value is desired) and (A positive value of MBE gives an overestimation in the predicted data and vice versa) [22].

$$MBE = \left[\sum \left(T_t - T_{exp} \right) \right]/n$$

3) Root mean square error, (RMSE). The lower the RMSE, the more accurate the model is. The sign of percentage errors is neglected [22].

$$RMSE = \left\{ \left[\sum \left(T_t - T_{exp} \right)^2 \right]/n \right\}^{1/2}$$

where,

T_{exp}: the reference experimental temperatures.

T_t: the model numerical temperatures.

n: number of temperature readings.

Tables 3-5 show the mean percentage error, the mean bias error, and the root mean square error of the MCHS model output temperatures for nodes at different depths when compared with related experimental data from the literature according to the key model parameters as shown below:

The lower MPE for nodes at 13 mm: $MPE_{13} = 4.14\%$ when using ranged thermal diffusivity.

The lower MPE for nodes at 32 mm: $MPE_{32} = 3.78\%$ when using ranged thermal diffusivity.

The lower MPE for nodes at 50 mm: $MPE_{50} = 13.62\%$ when thermal diffusivity $= 2.5 \times 10^{-7}$.

For the ranged thermal diffusivity: $MPE_{50} = 16.28\%$.

The lower MPE for nodes at 76 mm: $MPE_{76} = 6.73\%$ when using variable thermal diffusivity.

For the ranged thermal diffusivity: $MPE_{76} = 8.58\%$.

The accurate RMSE for nodes at 13 mm: $RMSE_{13} = 25.97$ °C when using ranged thermal diffusivity.

The accurate RMSE for nodes at 32 mm: $RMSE_{32} = 13.72$ °C when using ranged thermal diffusivity.

The accurate RMSE for nodes at 50 mm: $RMSE_{50} = 24.36$ °C when thermal diffusivity $= 2.0 \times 10^{-7}$.

For the ranged thermal diffusivity: $RMSE_{50} = 32.57$ °C.

The accurate RMSE for nodes at 76 mm: $RMSE_{76} = 19.71$ °C when using ranged thermal diffusivity.

Table 3. Accuracy statistical error analysis of MCHS temperature distribution with constant thermal diffusivity.

	MPE %			MBE °C			RMSE °C		
Constant α: $\times 10^{-7}$ (m²/sec)⟹	2.5	2.0	1.5	2.5	2.0	1.5	2.5	2.0	1.5
T-01 at 13 mm from the surface	4.79	6.07	12.39	13.38	−14.08	−50.92	30.25	33.44	62.54
T-02 at 32 mm from the surface	13	17.68	25.35	26.98	−9.23	−54.66	60.17	48.54	70.03
T-11 at 50 mm from the surface	13.62	16.67	29.49	29.43	−6.14	−48.29	50.19	24.36	52.99
T-03 at 76 mm from the surface	19.83	31.21	43.30	−13.70	−44.52	−78.37	21.67	50.91	95.78
The average values: ⟹	12.81	17.90	27.63	14	−18.49	−58.06	40.57	39.31	70.33

Table 4. Accuracy statistical error analysis of MCHS temperature distribution with ranged thermal diffusivity.

$\alpha_{i,j,t} = A \times \dfrac{e^{\left(-B \times time\right)}}{\left(3600 \times (T + 400)\right)}$	MPE %	MBE °C	RMSE °C
T-01 at 13 mm from the surface	4.14	0.88	25.97
T-02 at 32 mm from the surface	3.78	4.43	13.72
T-11 at 50 mm from the surface	16.28	23.93	32.57
T-03 at 76 mm from the surface	8.58	11.85	19.71
The average values: ⟹	8.19	10.27	22.99

Table 5. Accuracy statistical error analysis of MCHS temperature distribution with variable thermal diffusivity.

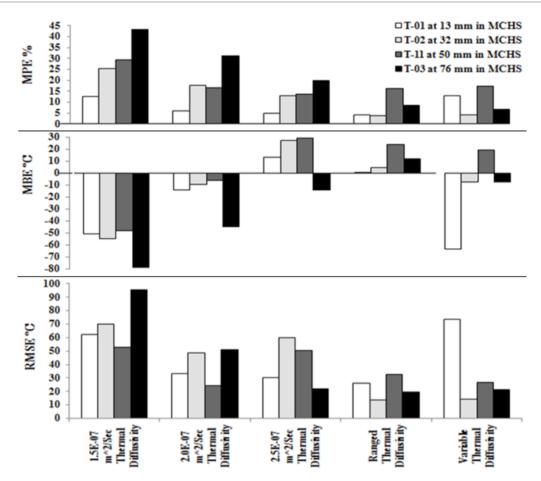| $\alpha_{i,j,t} = 0.01 \sqrt{(x^2 + y^2)} \dfrac{e^{\left(-0.1 \times time/60\right)}}{\left(3600 \times (T_{i,j,t} + 400)\right)}$	MPE %	MBE °C	RMSE °C
T-01 at 13 mm from the surface	13.02	−63.34	73.75
T-02 at 32 mm from the surface	4.08	−7.06	14.28
T-11 at 50 mm from the surface	17.36	19.30	26.72
T-03 at 76 mm from the surface	6.73	−7.36	21.45
The average values: ⟹	10.29	−14.61	34.05

Figure 15. Statistical error analysis for testing the accuracy of MCHS temperature distributionmodel output.

Figure 15 shows the statistical error analysis charts that present illustration and comparison to test the accuracy of the temperature distribution model output in MCHS with constant, ranged, and variable thermal diffusivities for nodes at different depths.

As shown in Figure 15, the lower RMSE and MBE values in the MCHS temperature distribution model output for the vast majority of nodes which represent the accurately predicted model results that are compared with related experimental data are achieved when using the ranged thermal diffusivity.

Furthermore, the averaged minimum MBE in MCHS corresponding to model output overestimation and underestimation is achieved for the vast majority of nodes by using ranged thermal diffusivity. The overall model accuracy is confirmed by the averaged minimum MPE % of all temperature nodes.

3.3 Characteristics of Response and Mechanical Performance Evaluation

The third subsection, finally, evaluates mechanical performance of the subjected HSCC fire response characteristics of constituent including:

1) Determining combined thermal properties at different depths for the subjected HSCC in a fire.

The main HSCC constituent materials response due to fire is the change in combined thermal properties (thermal diffusivities in m^2/sec). The adopted correlated thermal diffusivity MCHS model results are used to illustrate the change of thermal diffusivity as a function of temperature, time, and depth that varies for each node.

2) Determining the HSCC mechanical properties such as elasticity moduli, remaining strengths, and load distribution during the fire for both concrete and reinforcing steel.

In this paper, the Compression Strength and the Modulus of Elasticity for both steel reinforcement and concrete were considered as the mechanical performance criteria when evaluating the mechanical properties of the subjected HSCC in a fire.

The interface corner temperature of the node at 50 mm from the fire-exposed surfaces that resulted from a thermal branch of the model was used to calculate the remaining strengths according to Equations (13) and (14) for both

concrete and reinforcing steel bars.

Load distribution between steel reinforcement and concrete based on (MCHS). Basically, if a column of two different materials is subjected to a temperature rise under an axial load, at a certain temperature one of those materials will carry the total load [11,23].

3) Determining the subjected HSCC Rankine predicted failure load in the fire.

The proposed Rankine formula [15], according to Equations (17) to (23), assumes a linear interactive relationship between two failure modes of RCCs in a fire, these two modes are:

(1) **Crushing** for short columns (plastic squashing load causes compression failure).

The column is assumed to be short if the slenderness ratio is less than unity.

(2) **Buckling** for slender columns (elastic buckling load causes buckling failure).

The column is assumed to be slender (long) if the slenderness ratio is greater than unity.

For columns in the intermediate range where the slenderness ratio is close to unity, the failure occurs because the two modes, compression failure, and buckling failure, will interact with each other.

The subjected HSCC Rankine predicted failure load in the fire is calculated according to proposed correlations (17) to (23) by introducing the interface corner temperature that resulted from MCHS with ranged thermal diffusivity.

Figure 16a shows the change in combined thermal properties (thermal diffusivities in m^2/sec) at different depths versus time for the adopted MCHS when introducing ranged thermal diffusivity as a function of temperature and time that varies for each layer of depth.
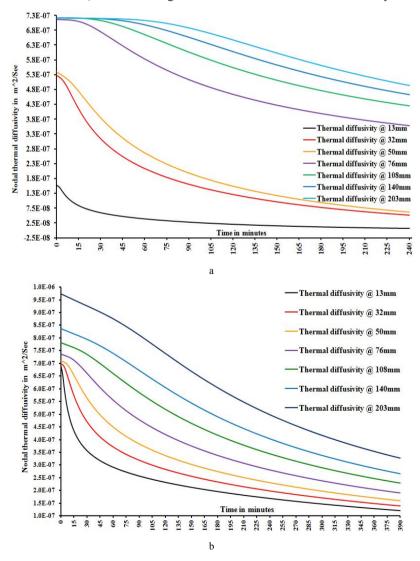

Figure 16. a) The change in ranged thermal diffusivities verses time for each layer of depth. b) The change in variable thermal diffusivities verses time for each node of depth.

Figures 16a and 16b show that the variation in the thermal diffusivity is solid evidence that proves that thermal and physical properties (K, Cp & p) of tested material HSC have to be changed.

Figures 17a and 17b show that the compression strength of concrete and compression strength of reinforcing steel bars are decreasing due to temperature increase because of fire exposure, on a base of interface corner node critical temperature MCHS model results when the thermal diffusivity is ranged versus corner critical interface temperature and time comparing with theoretical correlations proposed for RC under fire in reference [1].

The model predicted interface corner temperature was used in Equations (15) and (16) to determine the effective elastic moduli for both steel bars and concrete as shown below figures.

Figures 18a and 18b show the reduction in reinforcement steel and concrete elasticity moduli due to temperature increase because of fire exposure, based on interface corner critical temperature MCHS model results when the thermal diffusivity is constant, ranged, and variable versus time.
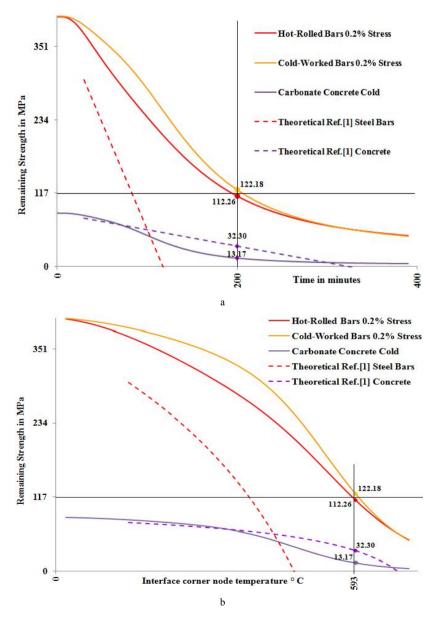

Figure 17. a) MCHS with ranged thermal diffusivity remaining strength VS time at interface-corner node. b) MCHS with ranged thermal diffusivity remaining strengths VS temperature at interface-corner node.

The time steps of model predicted middle and corner interface temperatures were used in Equations (17) ~ (23) to determine Rankine predicted failure load of RCC verses interfaces temperatures for the subjected HSCC in a fire exposure compared with the design load capacity of the subjected HSCC.

Figures 20a shows the load increase on reinforcing steel bars and the load decrease on concrete due to temperature increase because of fire exposure, based on interface corner critical temperature MCHS model results when the thermal diffusivity is constant, ranged, and variable versus time.

The above-shown data in Figure 20a can be utilized in the assessment of fire-damaged RC, especially for RCC and can be used in design procedures when accounting for fire resistance of HSCC.

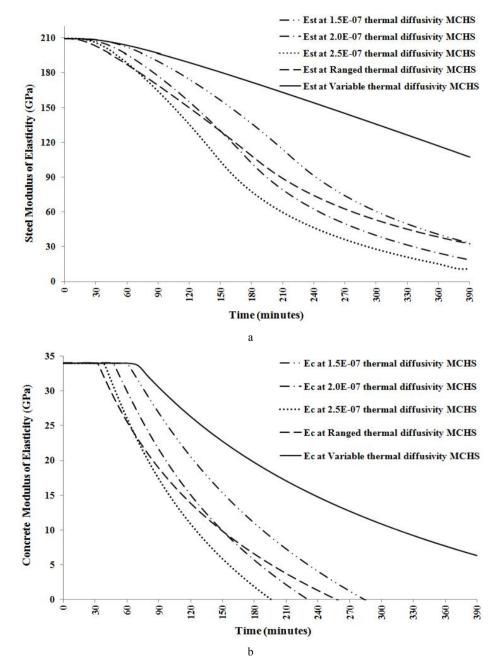For instance, Figure 20b shows that for the same spec-

a

b

Figure 18. a) Reduction in steel bars modulus of elasticity in MCHS vs. time. b) Reduction in concrete modulus of elasticity in MCHS vs. time.
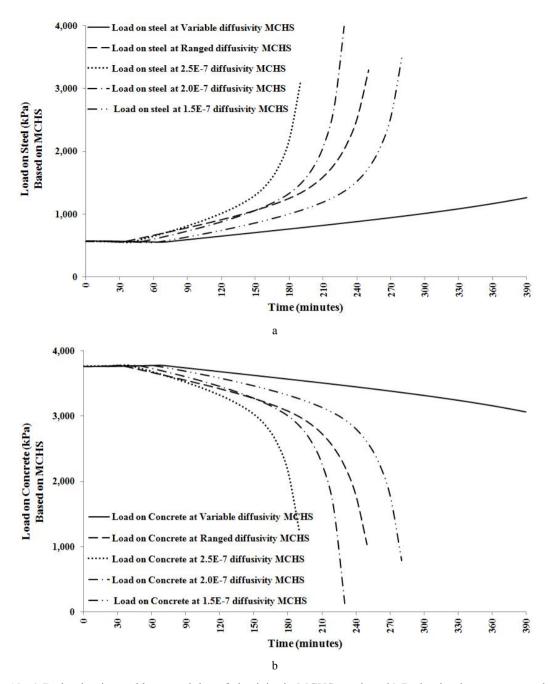
Figure 19. a) Reduction in steel bars modulus of elasticity in MCHS vs. time. b) Reduction in concrete modulus of elasticity in MCHS vs. time.

ification HSCC in the fire exposure scenario the subjected column with 4830 KN load capacity the estimated failure time of a similar column will be about 105 minutes of fire exposure.

Furthermore, if a similar column predicted fire failure load after 30 minutes is required, then it can be determined as shown in Figure 20b which is estimated at around 9470 KN.
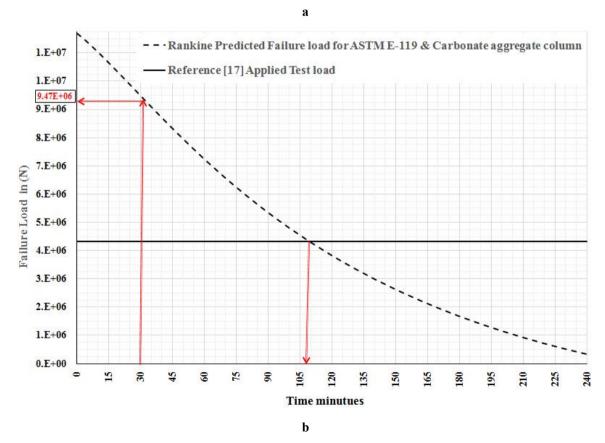
a

b

Figure 20. a) HSCC Rankine predicted failure load vs. interface temperatures in MCHS fire exposure. b) HSCC Rankine predicted failure load vs. time in MCHS fire exposure.

4. Conclusions

Based on the experimental and analytical results of this study, the following conclusions can be drawn:

1) The variation in the thermal diffusivity is solid evidence that proves that the thermal and physical properties (K, Cp & p) of the tested material (HSC) have been changed due to fire exposure. Therefore, the nodal temperature is a function of the heating period (time) and the location (depth) of each node. The resulting manipulated and refined correlations of the thermal diffusivity are valid in MCHS for the selected HSCC composed of carbonate aggregate in a hydrocarbon fire.

2) When the interface corner temperature reached 300 °C, the average reduction in steel reinforcing strength was approximately 16.5% and the average reduction in concrete strength was approximately 12%. At 500 °C, the average reduction in steel reinforcing strength was approximately 47.5% and the reduction in concrete strength was approximately 22%–62%. At 600 °C, the average reduction in steel reinforcing strength was approximately 71.11% and the reduction in concrete strength was approximately 40%–85%.

3) At 300 °C, the modulus of elasticity reduced by approximately 27% for concrete and reduced by approximately 11.4% for steel bars. While at 500 °C, the modulus of elasticity was reduced by approximately 64% for concrete and reduced by approximately 32% for steel bars. The effect of elevated temperature on the elastic modulus of elasticity is significant at 600 °C in concrete at 82% and in steel bars at 50%.

4) Two-dimension temperature distribution on HSCC exposed to MCHS in a fire has been predicated with an accuracy that is adequate using a developed simulation model.

5) The results of the thermal simulation branch were compared to previous experimental works and a very good level of agreement was obtained.

6) From the results of the mechanical evaluation branch, performance strength reduction charts were generated which take care of the effect of fire on reinforced concrete.

5. Recommendations

The summarized recommendations and suggestions can be into the following points:

1) The thermal diffusivity of the concrete as well as any other properties input model key parameters should reflect the physical situation. In other words, thermal diffusivity (a) in this study was correlated by the simplest proposed form for MCHS; however in reality it is a sharp function of temperature. This approximation had a pronounced impact on the accuracy of the results. This sensitivity of thermal diffusivity with temperature should be considered for other heating scenarios in any future research in order to observe the effect of this approximation.

2) As this study was based on published experimental work, it recommended that the experimental portion of the research should be performed to confirm this simulation results and another related theoretical study. This can be achieved through the availability of a fire lab to investigate the effect of elevated temperature on any concrete element under a load simulating real-life conditions, not only fixed ends and constant load conditions.

3) Sophisticated, specialized software is commercially-available that simulates the fire condition more comprehensively. However, due to the cost constraint, this software cannot be made available. It is recommended to analyse the effect of elevated temperature on the concrete structure when it is an entire multi-story building as opposed to just a single isolated concrete element. The authors of this study highly recommend the use of such simulation software in order to obtain results for many structural members of the fire-damaged building. This implementation might be of interest to future post-graduate studies as a joint research collaboration between the Departments of Civil Engineering and Mechanical Engineering.

4) Real fire-damaged building theoretical and practical methods of assessment research are highly recommended to be conducted to demonstrate the effect of fire on different types of buildings in Benghazi city after the war. Many of those inside the University of Benghazi.

Conflict of Interest

There is no conflict of interest.

References

[1] Abbasi, A., Hogg, P.J., 2005. A model for predicting the properties of the constitutes of a glass fiber rebar reinforced concrete beam at elevated temperature simulating a fire test. Composites Part B Engineering. 36(5), 384-393.
DOI: https://doi.org/10.1016/j.compositesb.2005.01.005

[2] Ali, F., Nadjai, A., Choi, S., 2010. Numerical and experimental investigation of the behavior of high strength concrete columns in fire. Engineering Structures. 32(5), 1236-1243.
DOI: https://doi.org/10.1016/j.engstruct.2009.12.049

[3] Kang, H.T., Chu, Y.T., 2002. A simple and rational approach for fire resistance prediction of rc columns.

Proceeding of the Second International Workshop "Structures in Fire".

[4] Bratina, S., Cas, B., Saje, M., et al., 2005. Numerical modelling of behavior of reinforced concrete columns in fire and comparison with Eurocode 2. International Journal of Solids and Structures. 42(21-22), 5715-5733.
DOI: https://doi.org/10.1016 /j.ijsolstr. 2005.03.015

[5] Wade, C.A., Cowles, G.S., Potter, R.J., et al., 1997. Concrete blade columns in fire. Concrete 97 Conference, Adelaide, Australia. Conference Proceedings.

[6] Espinos, A., Romero, M.L., Hospitaler, A., 2012. Simple calculation model for evaluating the fire resistance of unreinforced concrete filled tubular columns. Engineering Structures Journal. 42, 231-244.
DOI: https://doi.org/10.1016/j.engstruct.2012.04.022

[7] Ellingwood, B., Shaver, J.R., 1980. Effects of fire on reinforced concrete members. Journal of the Structural Division. 106, 2151-2166.

[8] Wickstrom, U., 1986. A very simple method for estimating temperature in fire exposed concrete structures. London and New York: Elsevier Applied Science Publishers.

[9] Kodur, V.R., Wang, T.C., Cheng, F.P., 2004. Predicting the fire resistance behaviour of high strength concrete columns. Cement & Concrete Composites. 26(2), 141-153.
DOI: https://doi.org/10.1016/S0958-9465(03)00089-1

[10] Federal Emergency Management Agency (FEMA), 2001. Structural Engineering Institute of the American Society of Civil Engineers (SEI/ASCE). World Trade Center Building Performance Study.

[11] Khanna, P.N., Punjab, P.W.D., 1997. Indian Practical Civil Engineering Hand Book.

[12] Kodur, V.R., Kacianauskas, R., Raftoyiannis, I.G., et al., 2014. Properties of concrete at elevated temperatures. International Scholarly Research Notices.
DOI: http://dx.doi.org/10.1155/2014/468510

[13] Dwaikat, M., Kodur, V.R., 2009. Hydrothermal model for predicting fire-induced spalling in concrete structural systems. Fire Safety Journal. 44(3), 425-434.
DOI: https://doi.org/10.1016/j.firesaf.2008.09.001

[14] Sethuraman, V.S., Suguna, K., 2016. Computation of modulus of elasticity of high strength concrete using silica fume. Asian Journal of Applied Sciences. 4(1), 54-62. Available from: www.ajouronline.com.

[15] Kodur, V.R., Dwaikat, M., Raut, N., 2009. Macroscopic fe model for tracing the fire responses of reinforced concrete structures. Engineering Structures. 31(10), 2368-2379.
DOI: https://doi.org/10.1016/j.engstruct.2009.05.018

[16] Kodur, V.R., Ahmed, A., Dwaikat, M., 2009. Modeling the fire performance of frp-strengthened reinforced concrete beams. Composites & Polycon. The American Composites Manufacturers Association (ACMA)'s annual convention and exhibition.

[17] Kodur, V.R., McGrath, R., Leroux, P., et al., 2005. Experimental studies for evaluating the fire endurance of hsc columns. National Research Council Canada.
DOI: https://doi.org/10.4224/20378032

[18] Yaqub, M., Bukhari, I.A., Ghani, U., 2012. Assessment of residual strength based on estimated temperature of post-heated rc columns. Journal of Engineering and Technology. 32(1), 55-70.

[19] Blagojevic, M.D., Pesic, D.J., 2011. A new curve for temperature-time relationship in compartment fire. Thermal Science. 15(2), 339-352.
DOI: https://doi.org/10.2298/TSCI100927021B

[20] Kumar, P., 2004. Rectangular rc columns subjected to fire load. Journal of the Institution of Engineers Civil Engineering Division Board. 85, 186-192.

[21] Hsu, J.H., Lin, Ch.Sh., Huang, Ch.B., 2005. Modeling the effective elastic modulus of rc beams exposed to fire. Journal of Marine Science and Technology. 14(2), 102-108.
DOI: https://doi.org/10.51400/2709-6998.2063

[22] Gopinathan, K.K., 1990. Solar radiation on inclined surfaces. Solar Energy. 45(I), 19-25.
DOI: https://doi.org/10.1016/0038-092X(90)90062-H

[23] Nash, W.A., 1984. Strength of materials. Civil Engineering Machaustus University, McGraw Hill, Dar Alraed Al-Arabie, Beirut—Lebanon, P.O. Box 6585, Telex L.E 43499.